Circular Microstructural Volume Elements with Periodic Boundary Conditions for Strain Localization Problems

P. Hofman

TU Delft

Circular Microstructural Volume Elements with Periodic Boundary Conditions for Strain Localization Problems

by

P. Hofman

to obtain the degree of Master of Science
at the Delft University of Technology,
to be defended publicly on Wednesday June 2, 2021 at 10:00 AM.

Student number:	4624068	
Project duration:	August 24, 2020 – June 2, 2021	
Thesis committee:	Dr. ir. F.P. van der Meer,	TU Delft, supervisor, chair
	Dr. S.R. Turteltaub,	TU Delft, supervisor
	L. Ke MSc,	TU Delft, daily supervisor

TU Delft

Abstract

A common choice for multiscale modeling of the mechanical response of composites is to use periodic boundary conditions (BCs) on square representative volume elements (RVEs). However, these periodic BCs over-constrain the response when strain localization takes place in bands that are not compatible with the imposed periodic constraints.

Previously developed improvements are based on aligning the periodic BCs with an evolving localization band. This is either done by applying a rotation to the periodicity frame or by imposing the periodic BCs in a weak sense and then applying a shift to the function that couples points. However, with matrix-inclusion RVEs, this change of the periodicity frame may cause a mis-alignment of inclusions that cross opposing edges, resulting in an artificial reinforcement along the RVE edge, which limits the number of supported localization angles and fails to provide a transversely isotropic response.

It is the objective of this thesis to develop a micromodel with transversely isotropic response for strain localization problems. It is shown that circular RVEs with straightforward application of periodic BCs provide a response which is independent of the load orientation but fail to predict full softening behavior. This is due to over-constraining when cracks reach the boundary. Therefore, a modification to the periodic BCs on a circular RVE is proposed, which allows for cracks to cross the edges. This is achieved by adding an unknown jump to the periodic constraint equations, which does not affect the response before localization. Moreover, a parameter that depends on the RVE size is used to make sure that the kinematics are consistent between scales in an average sense.

The performance of the formulation is tested with a series of simulations where macroscopic strain rates are imposed under varying angles. Additionally, a circular heterogeneous RVE with periodic material is presented where inclusions are allowed to cross the edge. It is demonstrated that the circular RVE with the modified periodic BCs successfully predicts an isotropic response with full softening.

In the simulations that were performed, *a priori* knowledge of the localization angle was used. However, the framework can be extended such that the BCs adapt to support an orientation of a localization band that is detected during the simulations.

Acknowledgement

First of all, I would like to express my sincere gratitude towards Dr. ir. Frans van der Meer, for his guidance, deep knowledge of the topic and for giving me the opportunity to work on a very interesting and open project. This gave me a taste of what science is truly about when there are no clear paths to take, which made my research much more exciting and motivating.

I would also like to thank Lu Ke, for his very valueable criticism and the encouraging words during our meetings.

Thanks are also directed to Dr. Sergio Turteltaub for being part of my committee and the interesting discussions on multiscale modeling.

Without a doubt, I would not have been able to do this work in these difficult times without my parents Peter and Martine. Thank you for your ever lasting support and for your patience by listening to my, and I apologise, way too extensive stories about circles and squares during the past nine months at the dinner table.

Sincere thanks to the Van der Velde family, Casper, Aya, Sil and Katja, for their many visits when I stayed in Drenthe and helping me with the groceries around the start of the pandemic.

Also, I am very grateful to my grandmother Tine Webeling, for her unconditional love and support throughout my life.

Special thanks go out to Bibian Tillema, for being in my life and for always believing in me. I feel very lucky knowing you.

Furthermore, I wish to thank Stan den Hartog, for being my friend and all the many laughs we had during and outside our studies, that started back in the days when we embarked on our engineering journey at the Hogeschool van Amsterdam.

Pieter Hofman
Amsterdam, May 2021

Contents

1 Introduction

1.1. General overview

Composites are materials that consist of two or more phases with different physical behavior. The overall effective properties of a composite material are largely dependent on the morphologies, the spatial distributions, the bonding between the constituents and the physics of the individual phases. With these composites, failure is initiated at the microscale where micro cracking starts and eventually multiple micro-cracks start to coalesce. When the loading increases, a macroscopic crack develops, which may lead to structural failure at the larger scale. This makes failure in composite materials an intrinsically multiscale phenomenon.

In order to improve the microstructure of the material to obtain desired characteristics or to verify its safety when it is used in structural applications, tests need to be performed for predicting the mechanical response when the material is subjected to load and environmental conditions. In theory, these tests could be carried out physically in a laboratory with an extremely large number of experiments in order to create phenomenological material laws. For materials with a complex microstructure and a response that is highly nonlinear and history dependent, it is practically impossible to perform physical experiments which consider all potential loading scenarios and corresponding failure mechanisms.

In cases where the information on the *true* physics of the constituents is available, virtual tests that are performed with computer simulations where the microstructure is explicitly modeled are more attractive. In virtual tests, it is possible to couple a macroscopic material point with a micromodel in which the heterogeneities are modeled in detail. Simulations are then performed simultaneously on both scales while information is exchanged in between, thereby replacing macroscopic material models.

The micromodel should accurately represent the microstructure (see Fig. 1.1), *i.e.* it should have enough constituents with the correct physical characteristics and the response must resemble the

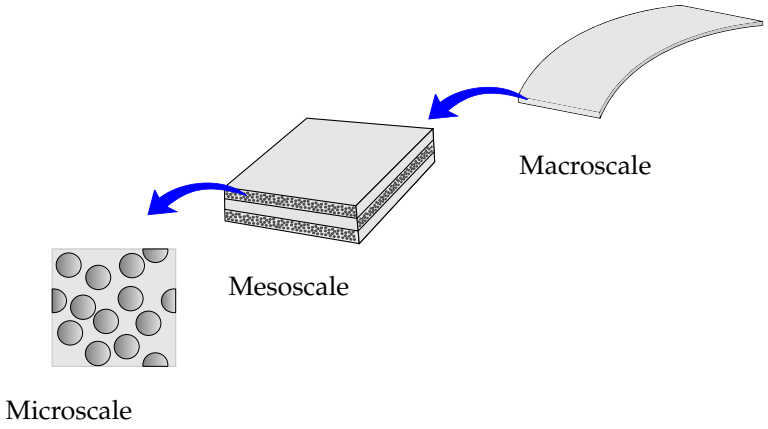

Figure 1.1: Three distinct scales of a composite laminate.

overall effective behavior accurately. If this is the case, the micromodel can be considered to be a *representative volume element* (RVE). In addition, the coupling between the macro and the micro model must be well defined. Usually, a macroscopic deformation is downscaled to the micromodel in the form of appropriate boundary conditions (BCs). After solving the micro boundary value problem (BVP), a homogenization procedure is performed to determine the overall response, which is usually obtained by taking the volume average of the stress in the RVE domain.

The most common type of BCs are periodic BCs on square RVEs. For microstructures with a regular orthogonal arrangement of inclusions, this choice leads to exact results. In the case of microstructures with a random distribution of inclusions, periodic BCs result in the fastest convergence with respect to increasing RVE sizes compared to other classical BCs [20]. However, when localization takes place in the micromodel, periodic BCs over-constrain the response since only crack bands that are aligned with the initial periodicity directions of the microstructure, are supported. The formulation of the microscale BVP with the applied periodic BCs is therefore *orientation dependent* and fails to accurately predict the isotropic response characteristic for random microstructures.

The formulation of appropriate BCs for strain localization problems is still an unresolved issue. In literature, several remedies are proposed to allow for arbitrary localization bands [24],[10],[2]. These approaches are essentially based on aligning the periodic constraints with (developing) localization bands. This is either done by applying a shift or a rotation to the function that couples opposing points. However, it is shown that this results in a mixed coupling of points that correspond to inclusions and matrix, leading to an artificial reinforcement along the RVE boundary and preventing RVE-wide crack bands to cross the edges [15].

Circular RVEs with periodic BCs are previously studied in [7] and seem to provide a promising alternative, since the RVE is intrinsically orientation independent due to its shape. However, the effectiveness of the BCs in representing complete failure of the material has not been proven.

1.2. Research objective

The goal of the research in this thesis is to develop a ***fully orientation independent micromodel*** which accurately predicts an isotropic response in strain localization analyses of composite materials.

This is achieved by exploring the use of circular RVEs and developing a new type of BCs specifically for the circular RVE which allow for fully localized deformations.

1.3. Thesis outline

The concepts of computational homogenization and the existing types of BCs are first discussed in the literature review in Chapter 2. In Chapter 3, the new formulation of the BCs on a circular RVE is presented and a methodology to test it is described in Chapter 4. In order to isolate the effect of the BCs on the response, a homogeneous RVE is first considered in Chapter 5. Since multiscale analyses are typically used for predicting the response of a random microstructure, a heterogeneous RVE is subsequently studied in Chapter 6. For this purpose, a circular heterogeneous RVE, where inclusions are allowed to cross the edge by exiting and re-appearing on the opposite side, is presented and subsequently used in the analyses. Finally, in Chapter 7, the main conclusions and recommendations for future research are addressed.

1.4. Notation

Superscripts M denote quantities with respect to the macro scale, while microscale quantities have no superscripts. Furthermore, tensor notation is used where bold-faced letters denote tensors, vectors and matrices.

Moreover, no distinction is made between material coordinates (reference configuration) and spatial coordinates (current configuration), since the small strains approach is used.

1.5. Implementation

The computational models are developed with the Jem/Jive C++ open-source toolkit from Dynaflow Research Group and implemented in the in-house Finite Element code of the computational mechanics group at the faculty of Civil Engineering and Geosciences at TU Delft. The heterogenous square and circular RVEs are created with a `python` code where the FE discretizations are generated with Gmsh [1].

2

Literature review

This chapter provides an overview of the currently existing multiscale frameworks. First, the most established classical computational homogenization, which is used in smooth problems where no sharp gradients exist in the solution field, is explored. In order to study problems which do have sharp gradients, more sophisticated approaches exist, which are briefly discussed. Since this work focuses on the application of appropriate boundary conditions, an overview of the classical and some special BCs is given. At the end of this chapter, the formulation from literature of periodic BCs on a circular RVE is discussed. It is demonstrated that the formulation fails to provide a full softening response. Therefore, a modification that resolves this issue is presented in the next chapter.

2.1. Computational homogenization

2.1.1. Classical computational homogenization

The main objective of homogenization in general is to determine the overall response of a heterogeneous material. A common approach is computational homogenization (CH) in which macroscopic material points (usually integration points) are properly coupled to microscopic BVPs, in which the heterogeneities of the material are fully resolved. The coupling serves as an algorithmic constitutive relation for the macro problem in which a kinematic quantity, *e.g.* the strain, coming from the macro scale, is downscaled to the micro model in the form of boundary conditions. Subsequently, the micro BVP is solved and the resulting homogenized stress and material tangent are upscaled to the macro scale (see Fig. 2.1 where this is schematized). The micro BVP therefore replaces a standard phenomenological constitutive relation between the macroscopic strains and stresses. In order to ensure that the energy transfer between both scales is consistent, the Hill-Mandel condition [11], also referred to as the macro-homogeneity condition, must hold. This condition is *a priori* satisfied with a proper application of boundary conditions and a definition of macroscopic stress as the volume average of the microscopic stress tensor.

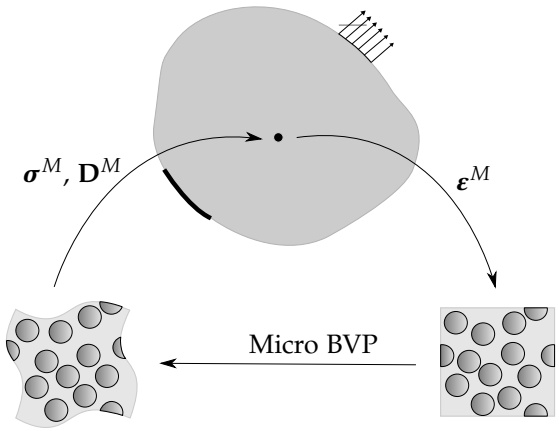

Figure 2.1: Multiscale scheme with classical computational homogenization.

Classical CH schemes are based on the assumption of a strict separation of scales where the principle requires that the scale of the microstructural fluctuation, l_{micro}, must be much smaller than the size of the RVE, l_{RVE}. In addition, the size of the RVE must be much smaller than the characteristic length over which the macroscopic fields vary, l_{macro} [5]. This is summarized in the following inequality

$$l_{micro} \ll l_{RVE} \ll l_{macro} \tag{2.1}$$

The first inequality needs to be satisfied in order to ensure that the RVE contains enough constituents to be statistically representative for the microstructure, such that the response will not change much upon increasing the RVE size. The second inequality is needed to ensure that the RVE represents a macroscopic material point where the deformation can be assumed to be constant. With this assumption, the upscaled response can be derived by imposing only the first gradient of the macroscopic displacement field onto an RVE. The displacement field inside the RVE domain is then a superposition of the smooth (linearly varying) macroscopic displacement field and a microfluctuation part that originates from the heterogeneities of the microstructure.

2.1.2. Computational homogenization for strain localization problems

When localization of deformation occurs, the assumption of separation of scales is violated and the micromodel cannot be considered to be statistically representative for the surrounding material anymore (only in the direction along the crack). Therefore, a microstructural volume element (MVE) as a term for the micromodel is often used instead. Secondly, the stress-strain response loses objectivity with respect to the RVE size [6]. When the RVE size is increased, the homogenized stress-strain response becomes more brittle since the energy dissipation in the localization band does not scale proportionally with the RVE size. Moreover, the macroscopic BVP becomes ill-posed and suffers from pathological mesh dependency since the homogenized stress-strain softening relation corresponds to a local damage model where the crack is smeared over the macroscopic elements.

To overcome these issues, discontinuous schemes are being developed where a discontuinuity,

e.g. with XFEM or zero-thickness interface elements, is inserted at the macroscale as soon as a certain failure criterion is reached, based on the homogenized quantities [26], [19]. In these approaches, the homogenized relation is a traction separation law (TSL) instead of a stress-strain law. Prior to localization, the macroscopic constitutive relation is linear elastic and comes from homogenization of the micro response, before the macro simulations are performed. At the onset of localization, the discontinuous homogenization scheme is adopted with nested micro BVP computations, replacing the macroscopic TSLs. As a result, this approach is only accurate when the nonlinear response prior to localization is negligible. In addition, it is only applicable when the loading history is not complex and there is no interest in the fine scale solution fields [20].

The drawbacks from the discontinuous schemes can be resolved by the introduction of a continuous-discontinuous approach in which the complex loading histories and strong non-linearities prior to localization are taken into account. Nguyen presented a method in [19] where an RVE, which is attached to a bulk integration point, is cloned after localization is detected and subsequently a crack is inserted at the macroscale. The RVE is then attached to the macro crack integration point, while the other bulk integration points are assumed to unload elastically. The homogenized macro response comes from averaging in a failure zone to ensure RVE size independence and is therefore mainly applicable with a continuum damage model on the micro scale.

More recently, several continuous-discontinuous schemes are developed in which *both* the bulk stress-strain *and* the crack traction-seperation laws come from nested micro BVPs attached to a single cohesive integration point ([4], [24], [3], [25], [21] to name a few). In these approaches, the first order classical CH is extended to the strain localization case with minimal changes to the first order CH framework. Therefore, almost the same procedures apply. The main differences are as follows:

- The downscaled macroscopic strain is replaced by an *equivalent* macro strain that consists of a bulk term and a volume averaged jump term.
- The averaging of the macroscopic jump term gives rise to a length scale parameter. This length scale parameter basically smears the macro jump over the micro RVE volume and plays an important role in removing the pathological dependence of the response on the RVE size and makes sure that energy transfer is consistent between both scales.
- Both the bulk stress-strain relation and a traction-separation law are obtained from the homogenization of nested micro BVPs, together with consistent tangent operators for both the bulk and cohesive IPs. The traction is obtained with the Cauchy theorem from the homogenized stress, which is the volume averaged micro stress.

The scale transition relations from classical CH, which to a large extent are similar to the continuous-discontinuous CH as mentioned above, are discussed in the next section.

2.2. Scale transition relations

2.2.1. Macro to micro

The macro and micro displacement fields in the RVE domain, denoted as Ω, can be expressed as

$$\boldsymbol{u}^M = \bar{\boldsymbol{u}} + \boldsymbol{H}^M \cdot \boldsymbol{x} \tag{2.2}$$

$$\boldsymbol{u} = \bar{\boldsymbol{u}} + \boldsymbol{H}^M \cdot \boldsymbol{x} + \tilde{\boldsymbol{u}} \tag{2.3}$$

where $\bar{\boldsymbol{u}}$ is a constant part of the macroscopic displacement field and where $\boldsymbol{H}^M$ is the macroscopic displacement gradient. It is implicitly assumed that the macroscopic deformation is constant inside the RVE domain, resulting in a linearly varying macroscopic displacement field in the RVE volume, which is consistent with the assumption of a strict separation of scales. The macro-to-micro scale transition is usually established with the requirement of an equal volume average, $\langle\cdot\rangle_\Omega \equiv \frac{1}{|\Omega|}\int_\Omega(\cdot)\,d\Omega$, of strains on both scales [13]

$$\langle\boldsymbol{\varepsilon}^M\rangle_\Omega \;=\; \langle\boldsymbol{\varepsilon}\rangle_\Omega \tag{2.4}$$

The macro and micro strain tensors can be obtained by applying the symmetric gradient operator $\boldsymbol{\nabla}^s(\cdot) \equiv \frac{1}{2}(\boldsymbol{\nabla}\otimes(\cdot) + (\cdot)\otimes\boldsymbol{\nabla})$ to the macroscopic and microscopic displacement fields (Eq. (2.2) and Eq. (2.3) respectively) and by considering that the macroscopic strain is constant in the RVE volume Ω. Therefore, Eq. (2.4) can be expressed as

$$\boldsymbol{\varepsilon}^M = \boldsymbol{\varepsilon}^M + \frac{1}{|\Omega|}\int_\Omega \boldsymbol{\nabla}^s\tilde{\boldsymbol{u}}\,d\Omega \tag{2.5}$$

from which it becomes apparent that the second term in the RHS must vanish such that Eq. (2.4) holds. Therefore, it is required that

$$\frac{1}{|\Omega|}\int_\Omega \boldsymbol{\nabla}^s\tilde{\boldsymbol{u}}\,d\Omega = 0 \tag{2.6}$$

This volume integral can be transformed into a surface integral with the divergence theorem, resulting in the following requirement for the microfluctuation along the boundary of the RVE $\partial\Omega$

$$\int_{\partial\Omega}\tilde{\boldsymbol{u}}\otimes^s\boldsymbol{n}\,d\partial\Omega = 0 \tag{2.7}$$

2.2.2. Micro to macro

When the boundary conditions, satisfying the kinematical requirement Eq. (2.14), are imposed on the RVE and the micro BVP is subsequently solved, the homogenized quantities are obtained from a micro-to-macro scale transition relation. For this purpose, the Hill-Mandel condition is used which ensures that the energy exchange is consistent between both scales. The requirement reads that the macro and micro power should be equal:

$$\langle P^M\rangle_\Omega = \langle P\rangle_\Omega \tag{2.8}$$

where P^M is the stress power at the macro scale and P is the stress power at the micro scale. This can be expressed as

$$\langle\boldsymbol{\sigma}^M : \dot{\boldsymbol{\varepsilon}}^M\rangle_\Omega = \langle\boldsymbol{\sigma} : \dot{\boldsymbol{\varepsilon}}\rangle_\Omega \tag{2.9}$$

When the microscopic strain expression is substituted in the RHS, this results in

$$\langle \boldsymbol{\sigma}^M : \dot{\boldsymbol{\varepsilon}}^M \rangle_\Omega = \langle \boldsymbol{\sigma} : \dot{\boldsymbol{\varepsilon}}^M + \boldsymbol{\sigma} : \dot{\boldsymbol{\nabla}^s} \tilde{\boldsymbol{u}} \rangle_\Omega \tag{2.10}$$

Without the presence of cracks inside the RVE and assuming that the RVE is in equilibrium, the second term in the RHS can be expressed in terms of a surface integral with the divergence theorem, resulting in the following requirement

$$\langle \boldsymbol{\sigma}^M : \dot{\boldsymbol{\varepsilon}}^M \rangle_\Omega = \langle \boldsymbol{\sigma} \rangle_\Omega : \dot{\boldsymbol{\varepsilon}}^M + \int_{\partial\Omega} \boldsymbol{t} \cdot \dot{\tilde{\boldsymbol{u}}} d\partial\Omega \tag{2.11}$$

Using the fact that the macroscopic stress and strain are constant inside the RVE volume, this becomes

$$\boldsymbol{\sigma}^M : \dot{\boldsymbol{\varepsilon}}^M = \langle \boldsymbol{\sigma} \rangle_\Omega : \dot{\boldsymbol{\varepsilon}}^M + \int_{\partial\Omega} \boldsymbol{t} \cdot \dot{\tilde{\boldsymbol{u}}} d\partial\Omega \tag{2.12}$$

This condition holds when the macroscopic stress definition is defined as the volume average of the stress in the RVE and when the BCs are such that the second term in the RHS vanishes

$$\boldsymbol{\sigma}^M \equiv \langle \boldsymbol{\sigma} \rangle_\Omega \tag{2.13}$$

$$\int_{\partial\Omega} \boldsymbol{t} \cdot \dot{\tilde{\boldsymbol{u}}} \, d\partial\Omega = 0 \tag{2.14}$$

For implementation, it is easier to transform the volume integral in Eq. (2.13) to a surface integral

$$\boldsymbol{\sigma}^M \equiv \frac{1}{|\Omega|} \int_\Omega \boldsymbol{\sigma} \, d\Omega = \frac{1}{|\Omega|} \int_{\partial\Omega} \boldsymbol{t} \otimes \boldsymbol{x} \, d\partial\Omega \tag{2.15}$$

where the microscale equilibrium equation and subsequently the divergence theorem is applied.

The discrete version of Eq. (2.15) is

$$\boldsymbol{\sigma}^M \equiv \frac{1}{|\Omega|} \sum_{i=1}^{\mathscr{B}} \boldsymbol{f}_i \otimes \boldsymbol{x}_i \tag{2.16}$$

where $\boldsymbol{f}_i$ are the nodal forces and $\mathscr{B}$ is the number of nodes on the boundary of the RVE.

In the next section, several approaches for satisfying the scale transition relations Eq. (2.7) and Eq. (2.14) are discussed.

2.3. Classical boundary conditions

There are multiple ways of imposing the macroscopic strain on a square RVE in the form of BCs. The most common BCs that are used in multiscale approaches are:

- Taylor BCs
- Linear BCs
- Periodic BCs
- Minimal kinematic BCs
- Traction BCs

It should be mentioned that uniform traction BCs are not suitable for analyses where the driving load is a macroscopic strain and not a macroscopic stress [13], and are therefore not discussed in the following.

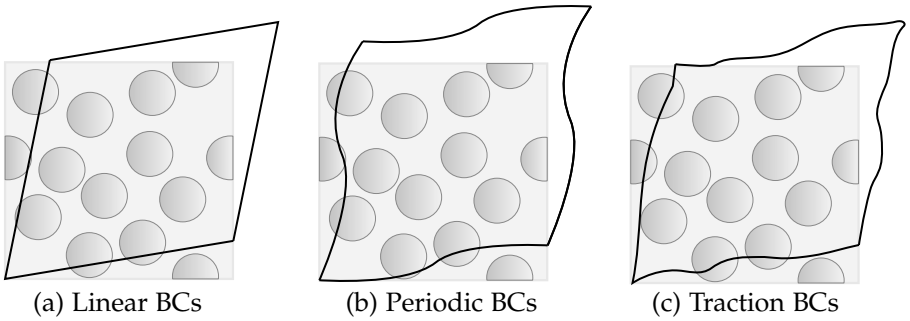

(a) Linear BCs (b) Periodic BCs (c) Traction BCs

Figure 2.2: Classical BCs and the allowed deformed shapes.

2.3.1. Taylor, linear and minimal kinematic BCs

In the case of the Taylor BCs, no microfluctation is assumed to exist in the RVE and the macroscopic linear displacement field given by Eq. (2.2) is directly applied on the entire volume of the RVE, where the rigid body motion (RBM) is removed without loss of generality.

$$\boldsymbol{u} = \boldsymbol{\varepsilon}^M \cdot \boldsymbol{x}, \qquad \boldsymbol{x} \in \Omega \tag{2.17}$$

The linear displacement BCs provide more kinematic freedom by allowing the microfluctuation to exist in the volume, but only vanish at the boundary of the RVE, such that Eq. (2.7) and Eq. (2.14) are satisfied.

$$\boldsymbol{u} = \boldsymbol{\varepsilon}^M \cdot \boldsymbol{x}, \qquad \boldsymbol{x} \in \partial\Omega \tag{2.18}$$

The simplest form of imposing the macroscopic strain is by directly enforcing Eq. (2.7), which provides the minimal kinematic BCs. It is shown in [18], that the minimal kinematic BCs [17] are the strain-controlled version of the traction BCs.

2.3.2. Periodic BCs

The most common way of imposing the transition requirements Eq. (2.7) and Eq. (2.14) is by applying a periodic microfluctuation field on opposing points along the boundary

$$\tilde{\boldsymbol{u}}^+ = \tilde{\boldsymbol{u}}^- \tag{2.19}$$

With Eq. (2.3) this can be rewritten in terms of total microscopic displacements (where the RBM is removed, as

$$\boldsymbol{u}^+ = \boldsymbol{u}^- + \boldsymbol{\varepsilon}^M \cdot (\boldsymbol{x}^+ - \boldsymbol{x}^-) \tag{2.20}$$

When periodic BCs are applied, it follows naturally that the traction is antiperiodic [9]. This should be the case since there are no applied external forces. Thus the RVE tractions, as a result of the constraints, must be in equilibrium.

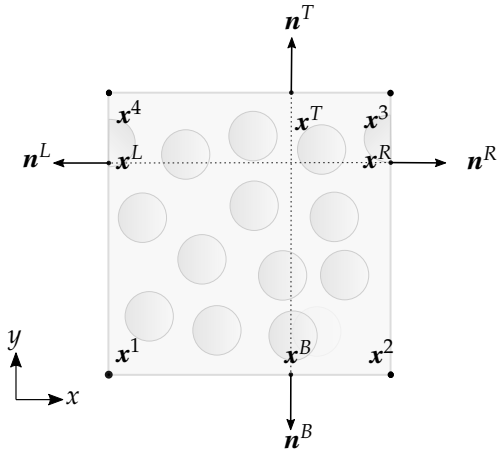

Figure 2.3: Schematic of the square RVE with periodic BCs.

From Eq. (2.19) and the fact that the normals along the boundary are antiperiodic, it follows that average strain consistency Eq. (2.7) is satisfied. In addition, for each pair of points on the boundary, it holds that $\boldsymbol{t}^+ = -\boldsymbol{t}^-$ and $\dot{\tilde{\boldsymbol{u}}}^+ = \dot{\tilde{\boldsymbol{u}}}^-$. Therefore the contribution of the microfluctuation, vanishes

$$\begin{aligned}\int_{\partial\Omega} \boldsymbol{t}\cdot\dot{\tilde{\boldsymbol{u}}} d\partial\Omega &= \int_{\partial\Omega^+} \boldsymbol{t}^+\cdot\dot{\tilde{\boldsymbol{u}}}^+ d\partial\Omega + \int_{\partial\Omega^-} \boldsymbol{t}^-\cdot\dot{\tilde{\boldsymbol{u}}}^- d\partial\Omega \\ &= \int_{\partial\Omega^+} \boldsymbol{t}^+\cdot\dot{\tilde{\boldsymbol{u}}}^+ + \boldsymbol{t}^-\cdot\dot{\tilde{\boldsymbol{u}}}^- d\partial\Omega = 0\end{aligned} \tag{2.21}$$

Since the relative coordinate vectors between pairs of nodes along each edge is constant, the constraint equations in Eq. (2.22) can be rewritten in terms of displacements of the corners nodes (see Fig. 2.3), resulting in

$$\begin{aligned}\boldsymbol{u}^T &= \boldsymbol{u}^B + \boldsymbol{\varepsilon}^M\cdot(\boldsymbol{x}^4 - \boldsymbol{x}^1) = \boldsymbol{u}^B + \boldsymbol{u}^4 - \boldsymbol{u}^1 \\ \boldsymbol{u}^R &= \boldsymbol{u}^L + \boldsymbol{\varepsilon}^M\cdot(\boldsymbol{x}^2 - \boldsymbol{x}^1) = \boldsymbol{u}^L + \boldsymbol{u}^2 - \boldsymbol{u}^1\end{aligned} \tag{2.22}$$

This allows for imposing any macroscopic strain by prescribing the nodal displacements of these corner nodes, which simplifies the implementation. In order to prevent rigid body translations, $\boldsymbol{u}^1$ is fixed.

2.3.3. Shortcomings of the classical BCs

It is generally known in the literature that the minimal kinematic BCs and the linear displacement BCs provide lower and upper bound estimates of the response respectively [2]. Since the RVE has a finite size and is assumed to be representative for a material point at the macroscale that is surrounded by other material, its response should ideally mimic this constraining effect of the surrounding material. The linear displacement BCs provide the most kinematic restriction by the surrounding material by only allowing a deformed RVE in which the edges are straight. For strain localization problems, this prevents a localization band to reach the boundary. The most kinematic freedom is provided by the minimal kinematic BCs. However, the response is sensitive to localization in zones near the boundary [2]. This leads to situations where the RVE already fails when small parts of the edges cut

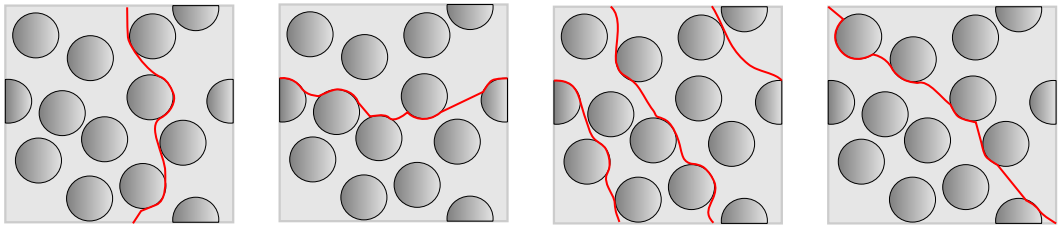

Figure 2.4: Supported localization patterns with periodic BCs.

loose. Furthermore, periodic BCs result in faster convergence in effective quantities with increasing RVE size compared to the linear BCs and the minimal kinematic BCs for random microstructures. In fact, for periodic microstructures the response is exact [12]. Moreover, periodic BCs allow for RVE-wide localization bands, although the bands have to fit the periodicity frame. See Fig. 2.2 for an overview of the deformed shapes that are allowed by the three classical BCs.

2.4. Special boundary conditions for strain localization problems

Periodic BCs lead to localization bands that are aligned with the periodic coupling directions. Therefore, only horizontal, vertical or a combination of inclined localization bands that are together periodic, may develop (see Fig. 2.4). This restricts the development of arbitrarily oriented single localization bands, which can result in a delay of macroscopic failure and generally leads to a spurious anisotropic response.

Several remedies have been proposed to resolve this issue. These are discussed in the sequel.

2.4.1. Aligned percolation path BCs

The first method is proposed by Coenen et al. and is termed the *aligned percolation path periodic BCs* [2]. In this approach, the periodicity frame is rotated with respect to the original microstructure periodicity directions and aligned with a developing localization band (see Fig. 2.5). Because of this, arbitrary localization band orientations are permitted by the RVE. The boundary conditions are defined as

$$\boldsymbol{u}^{l_N^+} = \boldsymbol{u}^{l_N^-} + \boldsymbol{\varepsilon}^M \cdot (\boldsymbol{x}^{l_N^+} - \boldsymbol{x}^{l_N^-}) \tag{2.23}$$

$$\boldsymbol{u}^{l_S^+} = \boldsymbol{u}^{l_S^-} + \boldsymbol{\varepsilon}^M \cdot (\boldsymbol{x}^{l_S^+} - \boldsymbol{x}^{l_S^-}), \qquad \text{if } \boldsymbol{n}^+ = -\boldsymbol{n}^- \tag{2.24}$$

$$\int_{\partial\tilde{\Omega}^{l_s}} (\boldsymbol{u}^{l_S^+} - \boldsymbol{u}^{l_S^-})\, d\partial\Omega = \boldsymbol{\varepsilon}^M \cdot \int_{\partial\tilde{\Omega}^{l_s}} (\boldsymbol{x}^{l_S^+} - \boldsymbol{x}^{l_S^-})\, d\partial\Omega, \quad \text{else} \tag{2.25}$$

These can be derived by multiplying Eq. (2.7) with the unit vectors that are parallel and perpendicular to a developing localization band. In the direction perpendicular to the strain localization band, the projected boundary is subdivided further into a part where the normals are anti-periodic and a part where they are not. A strong coupling is performed on parts of the boundary where the normals are anti-periodic and a weak coupling on the remaining part. This makes sure that the aligned percolation path BCs reduce to the periodic BCs when vertical and horizontal localization

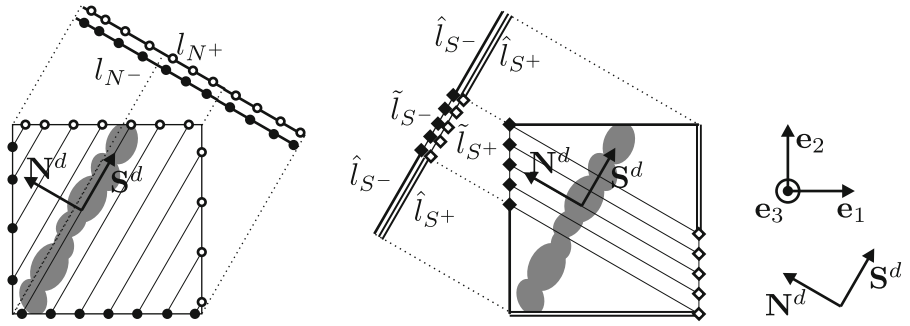

Figure 2.5: Aligned Percolation Path BCs [3].

bands develop.

The development of the localization band is tracked with an image processing tool (Hough transform) during the loading of the RVE. Therefore, the BCs have to be updated according to the direction of the most actively developing localization band. For a more elaborate derivation and details on the implementation the reader is referred to [2].

2.4.2. Aligned weakly periodic BCs

An alternative to the aligned percolation path BCs are the *aligned weakly periodic BCs* proposed by Svenning et al. [23]. Weakly periodic BCs were originally developed to allow for non-periodic meshes, therefore making the procedure of generating RVEs and adaptive mesh-refinement straightforward [14]. In this approach, the periodicity of microfluctuations is imposed in a weak sense with Lagrange multipliers, which can be interpreted as an unknown traction in the microscale weak form. Therefore, this approach constitutes a mixed formulation in which the boundary displacements as well as the tractions are unknowns. It is shown in [22] that weakly periodic BCs allow partial cracks (cracks that do not run through the entire RVE) at the RVE boundary, since the traction approximation can be made discontinuous along the crack. Moreover, weakly periodic BCs allow for a transition between the strong (point-wise) periodic BCs and the minimal kinematic BCs by coarsening the traction approximation. More interestingly, in a more recent article [24], it is shown that the weakly periodic BCs allow for aligning the BCs with a preferential localization direction by simply adding a translational shift to the function that couples opposing nodes on the boundary. With this approach, an inclined localization band is compatible with the shifted periodicity frame of the microstructure. A short description of the boundary conditions is provided for completeness in the following. For a more detailed description see [14], [22], [23].

The weak formulation of the periodicity of microfluctuations is given in terms of total micro displacements as

$$\int_{\partial\Omega^+} \delta \boldsymbol{t}_\lambda \cdot (\boldsymbol{u}^+ - \boldsymbol{u}^-)\, d\partial\Omega = \int_{\partial\Omega^+} \delta \boldsymbol{t}_\lambda \cdot \boldsymbol{\varepsilon}^M \cdot (\boldsymbol{x}^+ - \boldsymbol{x}^-)\, d\partial\Omega \tag{2.26}$$

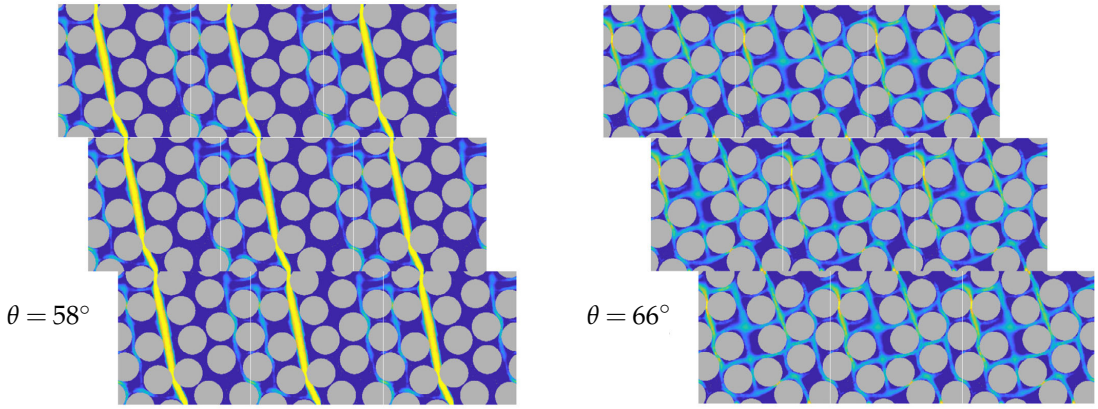

Figure 2.6: Geometric artifacts as a result of a shift to the periodicity frame [15]. Note that a mis-alignment of fibers prevents the localization band to cross the boundary when $\theta = 66°$.

The quasi-static weak form of the microscale BVP (in the absence of body forces) is given as

$$\int_{\Omega} \boldsymbol{\sigma} : \delta\boldsymbol{\varepsilon} \, d\Omega - \int_{\partial\Omega^+} \boldsymbol{t}_\lambda \cdot (\delta\boldsymbol{u}^+ - \delta\boldsymbol{u}^-) \, d\partial\Omega = 0 \tag{2.27}$$

where the anti-periodicity of tractions is used. The derivation can be obtained by multiplying Eq. (2.22) with the Lagrange multiplier, denoted as $\delta\boldsymbol{t}_\lambda$, and subsequently integrating over the RVE edge. Furthermore, these constraints can conveniently be aligned when a translational shift is applied to the mapping between two opposing points $\boldsymbol{u}^+$ and $\boldsymbol{u}^-$.

In a recent article by Giesen Loo and Van der Meer [15], the formulation of the aligned weakly periodic BCs is extended such that it can be used in stress controlled simulations. In addition, an isotropy study is performed in which it is demonstrated that aligned weakly periodic BCs do not consistently perform well for arbitrary localization angles when it is applied to fiber-matrix RVEs. For some orientation angles, the shift in the microstructure results in a mis-alignment of fibers that cross the edge. From Fig. 2.6 it can be observed that these artifacts prevent a clean localization band to cross the boundaries when $\theta = 66°$.

This issue can be alleviated by considering RVEs with fibers that cannot cross the boundary. However, this results in undesired *wall-effects* [6], which is physically unrealistic since the RVE must represent a material point of an infinite system. Using larger sized RVEs also alleviates the issue, since the chance of mis-aligned fibers preventing a crack to cross the edges, becomes smaller.

Another issue with these BCs is that the alignment angle must be *a priori* known since it affects the response, also before localization occurs. In realistic situations where the localization direction is not known *a priori* , adapting the alignment angle during simulations results in sudden changes in the BCs which can lead to convergence issues because the reaction forces abruptly change.

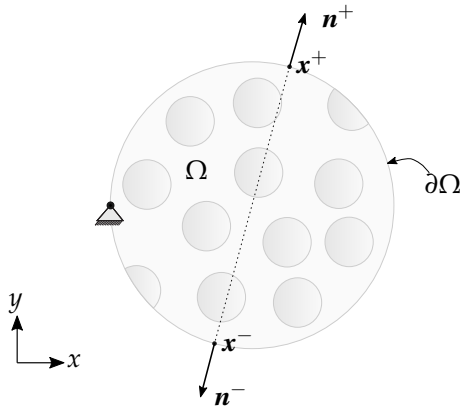

Figure 2.7: Schematic of the circular RVE with periodic BCs.

2.5. Periodic BCs on circular RVEs

Glüge et al. discussed the applicability of spherical RVEs in the context of numerical homogenization (NH), where the overall behavior of the heterogeneous material is *a posteriori* determined from single-scale micromechanical analyses [9], [8].

In order to apply periodic BCs such that the kinematical averaging relation Eq. (2.4) holds, it is required that coupled points have anti-periodic normals ($\boldsymbol{n}^+ = -\boldsymbol{n}^-$) such that the contribution of the microfluctuation to the average strain Eq. (2.7) and average microscopic power Eq. (2.14) vanishes.

The periodicity of microfluctuations is then enforced by applying the following BCs on the circular RVE edge

$$\boldsymbol{u}^+ = \boldsymbol{u}^- + \boldsymbol{\varepsilon}^M \cdot (\boldsymbol{x}^+ - \boldsymbol{x}^-), \qquad \boldsymbol{x} \in \partial\Omega^+ \tag{2.28}$$

A schematic of the application of Eq. (2.28) on a two-dimensional circular RVE with domain Ω and external boundary $\partial\Omega$ is shown in Fig. 2.7. It should be noted that the macroscopic strain must be imposed directly on each pair of nodes. It is not possible to use control (corner) nodes as commonly performed with the square RVE, since the relative coordinate vector connecting opposing nodes is different for each pair, which results in the inability of expressing the inhomogeneous side of the constraint equations in terms of control displacements. In order to prevent rigid body translations, one node is fixed.

In the following it is demonstrated that the circular RVE with periodic BCs leads to severe over-constraining in the softening branch, since the BCs do not allow for a complete separation in two unloaded parts. For this purpose, an analytical case is presented, where it is demonstrated that a realistic failure mode is not supported by the imposed constraints.

Consider a uniaxial strain of $\varepsilon^M_{xx} \neq 0$, $\varepsilon^M_{xy} = \varepsilon^M_{yx} = 0$, $\varepsilon^M_{yy} = 0$, that is imposed on the RVE via Eq. (2.28). The ultimate failure mode (with a fully developed crack and two unloaded hemicircles) is shown in Fig. 2.8. The application of the periodic BCs on two arbitrary node pairs $\{\boldsymbol{x}^-_\alpha, \boldsymbol{x}^+_\alpha\}$ and $\{\boldsymbol{x}^-_\beta, \boldsymbol{x}^+_\beta\}$ in x-direction leads to

$$u^+_{\alpha x} - u^-_{\alpha x} = \varepsilon^M_{xx}(x^+_\alpha - x^-_\alpha) \tag{2.29}$$

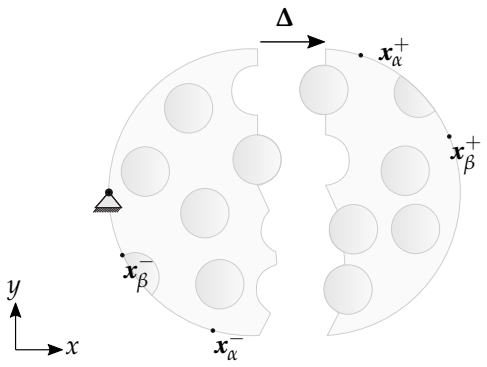

Figure 2.8: Preferred ultimate failure mode with the circular RVE.

$$u_{\beta x}^{+} - u_{\alpha x}^{-} = \varepsilon_{xx}^{M}(x_{\beta}^{+} - x_{\beta}^{-}) \tag{2.30}$$

From the figure, it can be observed that the deformed mode corresponds to $u_{\alpha x}^{+} = \Delta$, $u_{\beta x}^{+} = \Delta$ and $u_{\alpha x}^{-} = 0$, $u_{\beta x}^{+} = 0$. Substituting these in Eq. (2.28) for both node pairs yields

$$\Delta = \varepsilon_{xx}^{M}(x_{\alpha}^{+} - x_{\alpha}^{-}) \tag{2.31}$$

$$\Delta = \varepsilon_{xx}^{M}(x_{\beta}^{+} - x_{\beta}^{-}) \tag{2.32}$$

Since $x_{\alpha}^{+} - x_{\alpha}^{-} \neq x_{\beta}^{+} - x_{\beta}^{-}$, there exists no value for ε_{xx}^{M} for which Eq. (2.31) and Eq. (2.32) are both satisfied. Therefore, a deformation mode that corresponds to complete separation in two parts of the RVE is not supported by the imposed constraints. This makes the formulation unsuitable for the analysis of localization problems.

2.6. Concluding remarks

The classical periodic BCs do not allow for arbitrary localization angles. Both the aligned weakly periodic BCs and the aligned percolation path BCs require a shifting or rotation of the periodicity frame.[1] Moreover, aligned percolation path BCs are not fully orientation independent: with inclined bands, a weak coupling is imposed on a part of the RVE edge where node pairs cross the discontinuity, which is not the case with horizontal or vertical localization bands where the formulation reduces to strong periodic BCs.

Circular RVEs with periodic BCs are attractive, because of the intrinsic orientation independent shape. However, it is demonstrated with an analytical example in Sec. 2.5 that the existing BCs on circular RVEs prevent a realistic failure mode. Based on these findings there is a need for an improvement to the formulation. A novel framework for the circular RVE and new BCs is presented in the next chapter.

[1] Aligned percolation path BCs have only been studied in combination with voided microstructures without material periodicity in [2],[4]. However, it is expected that the approach is not suitable for matrix-fiber RVEs where periodicity of material is taken into account in order to avoid *wall-effects*, because of the same reasons as with the aligned weakly periodic BCs.

3

Formulation of the new BCs

It has been demonstrated in the previous chapter that periodic BCs imposed on a circular RVE suppress the development of a complete softening response. Therefore, a modification to the periodic BCs is presented in this chapter.

The analytical example in Sec. 2.5 showed that the origin of the over-constraining is directly related to the inhomogeneous part in the constraint equations (Eq. (2.28)). Since a uniform macroscopic deformation field is imposed, the inhomogeneous part scales with the distance vector between the nodes. However, when localization of deformation occurs in the RVE, this assumption is invalid. Instead, a (constant) jump is required between pairs of nodes that exist on either side of the discontinuity, which cannot be achieved with the standard periodic coupling on the circular RVE boundary.

A mathematical explanation is provided in this section, by closely examining the scale transition relations. In the case of most of the FE^2 schemes for strain localization problems (see Sec. 2.1.2), an equivalent macroscopic strain is imposed on the RVE in an averaged sense. This equivalent macroscopic strain is composed of a macro bulk strain and a macro jump, averaged over the microscopic RVE volume. When the equivalent macroscopic strain is imposed on the RVE after localization, the microscopic displacement field is a superposition of a linearly varying part, a *smooth* fluctuating microscopic part due to the heterogeneities and a (sharp) jump (see Fig. 3.1).

It is proposed in this work to *only* let the smooth microfluctuation part, that is due to the heterogeneities, vanish along the circular RVE. Simultaneously, it is shown that consistency of average strain on both scales is still maintained. This can be achieved by modifying the periodic BCs such that an (unknown) jump term is added to the periodic constraint equations, thereby providing extra kinematic freedom which allows for a full softening response.

In the following, the newly proposed periodic BCs are denoted as *modified periodic boundary conditions* (*mod*-PBCs), while the standard periodic BCs by Glüge et al. are denoted as (*std*-PBCs).

3.1. Mathematical formulation

3.1.1. Macroscale

When sharp strain localization occurs, the macro displacement field (without rigid body translations) in the microstructural volume can be expressed as

$$\boldsymbol{u}^M = \boldsymbol{H}^M \cdot \boldsymbol{x} + \mathcal{H}^M [\![\boldsymbol{u}]\!]^M \tag{3.1}$$

where $\boldsymbol{H}^M$ is the macroscale displacement gradient, $\mathcal{H}^M$ is the Heaviside function active at the discontinuity Γ^M and $[\![\boldsymbol{u}]\!]^M$ denotes the jump. In the context of small strains, applying the symmetric gradient operator, $\boldsymbol{\nabla}^s(\cdot) \equiv \frac{1}{2}(\boldsymbol{\nabla} \otimes (\cdot) + (\cdot) \otimes \boldsymbol{\nabla})$, to the displacement field on the macroscale yields the macro strains

$$\boldsymbol{\varepsilon}^M = \boldsymbol{\nabla}^s \boldsymbol{u}^M = \boldsymbol{\varepsilon}_b^M + \delta_\Gamma^M [\![\boldsymbol{u}]\!]^M \otimes^s \boldsymbol{n}_\Gamma^M \tag{3.2}$$

In this equation, $\boldsymbol{\varepsilon}_b^M$ is the macroscale bulk strain and δ_Γ^M denotes a sharp Dirac function that is active at the discontinuity Γ^M. Subsequently, a macroscopic *equivalent* strain $\boldsymbol{\mathcal{E}}^M$ is imposed on the RVE and drives the deformation. This quantity is constructed as the volume average, $\langle\cdot\rangle_\Omega \equiv \frac{1}{|\Omega|}\int_\Omega (\cdot)\, d\Omega$, of the macroscopic strain, implying a macro jump that is smeared over the RVE volume

$$\boldsymbol{\mathcal{E}}^M \equiv \langle \boldsymbol{\varepsilon}^{\boldsymbol{M}} \rangle_\Omega = \boldsymbol{\varepsilon}_b^M + \frac{|\Gamma|}{|\Omega|} [\![\boldsymbol{u}]\!]^M \otimes^s \boldsymbol{n}_\Gamma^M \tag{3.3}$$

Note that the Dirac property $\int_\Omega f(\boldsymbol{x}) \delta_\Gamma \, d\Omega = \int_\Gamma f(\boldsymbol{x}_\Gamma) \, d\Gamma$ is used and the macroscopic jump and normal vector of the discontinuity are assumed to be constant over the RVE volume. In addition, it is assumed that the center of the microscopic circular domain is positioned such that the (straight) macroscopic discontinuity crosses the RVE edge at two points with anti-periodic normal vectors. Therefore, $|\Gamma| = 2R$, where R is the radius of the circular RVE.

3.1.2. Microscale

The microscale displacement field after localization can be expressed as

$$\boldsymbol{u} = \boldsymbol{\mathcal{E}}^M \cdot \boldsymbol{x} + \underbrace{\hat{\tilde{\boldsymbol{u}}} + \bar{\tilde{\boldsymbol{u}}}}_{\tilde{\boldsymbol{u}}} \tag{3.4}$$

where it consists of the macroscopic *equivalent* strain $\boldsymbol{\mathcal{E}}^M$ (as defined in Eq. (3.3)) that is imposed on the RVE and the *total* microfluctations $\tilde{\boldsymbol{u}}$ (see Fig. 3.1). Furthermore, the *total* microfluctuation $\tilde{\boldsymbol{u}}$ is split into two separate contributions $\hat{\tilde{\boldsymbol{u}}}$ and $\bar{\tilde{\boldsymbol{u}}}$ representing the *sharp* and the *smooth* part respectively. The *sharp* part is related to the localization on the microscale and the *smooth* part to the heterogeneities.

In order to dissect the microflucations in two contributions, it is convenient (as shown in Sec. 3.1.3) to express the *sharp* part of the microfluctuation as

$$\hat{\tilde{\boldsymbol{u}}} = \mathcal{H}[\![\boldsymbol{u}]\!] - \frac{1}{\gamma} [\![\boldsymbol{u}]\!] \otimes^s \boldsymbol{n}_\Gamma \cdot \boldsymbol{x} \tag{3.5}$$

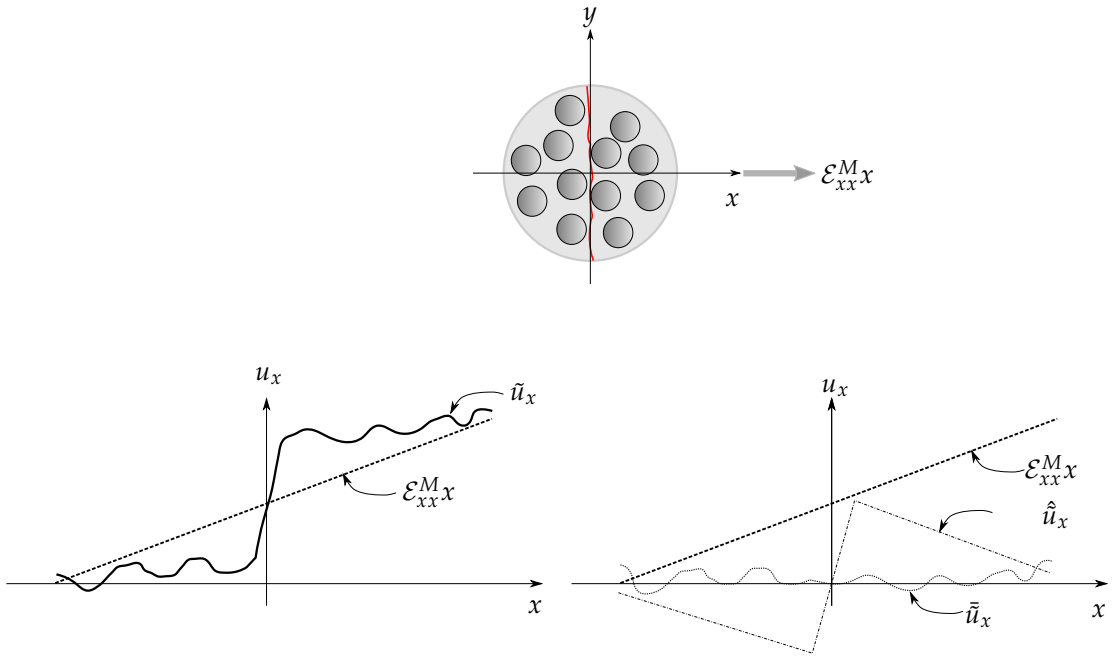

Figure 3.1: Decomposition of the micro displacement field along the x-direction when a macroscopic uniaxial strain is imposed on the RVE.

where $\mathcal{H}$ is a regularized Heaviside function.[1] The parameter γ is introduced to ensure average strain consistency, as will be clarified in Sec. 3.1.3.

Applying the symmetric gradient operator on the microscale displacement field yields the microscale strain field

$$\boldsymbol{\varepsilon} = \boldsymbol{\mathcal{E}}^M + \boldsymbol{\nabla}^s \hat{\hat{\boldsymbol{u}}} + \boldsymbol{\nabla}^s \bar{\tilde{\boldsymbol{u}}} \tag{3.6}$$

Substitution of the expression of the *sharp* microfluctuation Eq. (3.5) in the second term on the RHS gives

$$\boldsymbol{\nabla}^s \hat{\hat{\boldsymbol{u}}} = \delta_\Gamma [\![\boldsymbol{u}]\!] \otimes^s \boldsymbol{n}_\Gamma - \frac{1}{\gamma} [\![\boldsymbol{u}]\!] \otimes^s \boldsymbol{n}_\Gamma \tag{3.7}$$

where δ_Γ is a regularized Dirac function, active at the microscale discontinuity Γ. Note that it is again assumed that the micro jump and the corresponding normal vector are constant in the RVE.

3.1.3. Constructing the BCs

The equivalence of total average strain between both scales is used to construct the BCs and impose the macroscale deformation on the RVE.

$$\langle \boldsymbol{\varepsilon}^M \rangle_\Omega = \langle \boldsymbol{\varepsilon} \rangle_\Omega \tag{3.8}$$

Which can be evaluated as

[1] Since a fracture energy regularized continuum damage model (CDM) is adopted on the microlevel, that smears the displacement jump over the element.

$$\boldsymbol{\mathcal{E}}^M = \langle \boldsymbol{\mathcal{E}}^M + \delta_\Gamma [\![\boldsymbol{u}]\!] \otimes^s \boldsymbol{n}_\Gamma - \frac{1}{\gamma} [\![\boldsymbol{u}]\!] \otimes^s \boldsymbol{n}_\Gamma + \boldsymbol{\nabla}^s \bar{\tilde{\boldsymbol{u}}} \rangle_\Omega \tag{3.9}$$

After performing the integrations in the RHS, this results in

$$\boldsymbol{\mathcal{E}}^M = \boldsymbol{\mathcal{E}}^M + \frac{|\Gamma|}{|\Omega|} [\![\boldsymbol{u}]\!] \otimes^s \boldsymbol{n}_\Gamma - \frac{1}{\gamma} [\![\boldsymbol{u}]\!] \otimes^s \boldsymbol{n}_\Gamma + \langle \boldsymbol{\nabla}^s \bar{\tilde{\boldsymbol{u}}} \rangle_\Omega \tag{3.10}$$

where the Dirac property is again used and where it is assumed that the microjump $[\![\boldsymbol{u}]\!]$ and the micro normal $\boldsymbol{n}_\Gamma$ are constant. It can be observed from this expression that average strain is conserved when two requirements are met: (i) $\gamma = \frac{|\Omega|}{|\Gamma|}$, (ii) the contribution from the *smooth* microfluctuation to the average strain tensor vanishes along the boundary.

This choice for γ is crucial in correctly imposing the *equivalent* macroscopic deformation, in order to satisfy average strain equivalence. Using the divergence theorem, the last expression in the RHS of Eq. (3.10) can be expressed as an integral over the RVE boundary.

$$\int_\Omega \boldsymbol{\nabla}^s \bar{\tilde{\boldsymbol{u}}} d\Omega = \int_{\partial\Omega} \bar{\tilde{\boldsymbol{u}}} \otimes^s \boldsymbol{n} \, d\Omega = 0 \tag{3.11}$$

This expression can be satisfied by requiring that the *smooth* microfluctuations are periodic on opposing points where the normal vectors are anti-periodic (see Fig. 2.7). Note that the distinct feature of the approach presented here, is that *only* this part of the microfluctuation is periodic. This makes sense since the *smooth* part originates from the heterogeneities, and the sharp part is also present on the macroscale.

Thus, requiring $\bar{\tilde{\boldsymbol{u}}}^+ = \bar{\tilde{\boldsymbol{u}}}^-$ with $\boldsymbol{n}^+ = -\boldsymbol{n}^-$ for each pair of nodes satisfies Eq. (3.11). Evaluating Eq. (3.4) on the RVE edge on both the positive and the negative side of the discontinuity respectively yields

$$\boldsymbol{u}^+ = \boldsymbol{\mathcal{E}}^M \cdot \boldsymbol{x}^+ + \hat{\tilde{\boldsymbol{u}}}^+ + \bar{\tilde{\boldsymbol{u}}}^+ \tag{3.12}$$

$$\boldsymbol{u}^- = \boldsymbol{\mathcal{E}}^M \cdot \boldsymbol{x}^- + \hat{\tilde{\boldsymbol{u}}}^- + \bar{\tilde{\boldsymbol{u}}}^- \tag{3.13}$$

Substracting both expressions gives

$$\boldsymbol{u}^+ - \boldsymbol{u}^- = \boldsymbol{\mathcal{E}}^M \cdot (\boldsymbol{x}^+ + \boldsymbol{x}^-) + \hat{\tilde{\boldsymbol{u}}}^+ - \hat{\tilde{\boldsymbol{u}}}^- + \cancelto{0\ (\textit{mod}\text{-PBCs})}{\bar{\tilde{\boldsymbol{u}}}^+ - \bar{\tilde{\boldsymbol{u}}}^-} \tag{3.14}$$

where the *smooth* parts of the microfluctuation cancel out because of the requirement of periodic *smooth* microfluctuations. Evaluating the sharp contributions Eq. (3.5) at the associated $(+)$ and $(-)$ sides gives

$$\hat{\tilde{\boldsymbol{u}}}^- + \bar{\tilde{\boldsymbol{u}}}^- = (\mathcal{H}^+ [\![\boldsymbol{u}]\!] - \frac{1}{\gamma} [\![\boldsymbol{u}]\!] \otimes^s \boldsymbol{n}_\Gamma \cdot \boldsymbol{x}^+) - (\mathcal{H}^- [\![\boldsymbol{u}]\!] - \frac{1}{\gamma} [\![\boldsymbol{u}]\!] \otimes^s \boldsymbol{n}_\Gamma \cdot \boldsymbol{x}^-) \tag{3.15a}$$

$$= [\![\boldsymbol{u}]\!] - \frac{1}{\gamma} [\![\boldsymbol{u}]\!] \otimes^s \boldsymbol{n}_\Gamma \cdot (\boldsymbol{x}^+ - \boldsymbol{x}^-) \tag{3.15b}$$

After substitution of this in Eq. (3.14), it follows that

$$\boldsymbol{u}^+ - \boldsymbol{u}^- = \boldsymbol{\mathcal{E}}^M \cdot (\boldsymbol{x}^+ + \boldsymbol{x}^-) + [\![\boldsymbol{u}]\!] - \frac{1}{\gamma} [\![\boldsymbol{u}]\!] \otimes^s \boldsymbol{n}_\Gamma \cdot (\boldsymbol{x}^+ - \boldsymbol{x}^-) \tag{3.16}$$

which can be rewritten as

$$\boldsymbol{u}^+ = \boldsymbol{u}^- + (\boldsymbol{\mathcal{E}}^M - \frac{1}{\gamma}[\![\boldsymbol{u}]\!] \otimes^s \boldsymbol{n}_\Gamma) \cdot (\boldsymbol{x}^+ - \boldsymbol{x}^-) + [\![\boldsymbol{u}]\!] \tag{3.17}$$

resulting in the new *mod*-PBCs. The implementation details of these BCs are provided in the next section. Note that prior to localization, the microjump $[\![\boldsymbol{u}]\!]$ is zero and Eq. (3.17) reduces to the *std*-PBCs Eq. (2.28). Therefore, the extra kinematic freedom is only utilized when necessary.

Also notice that a failure mode which consists of two (fully unloaded) halves of the RVE (Fig. 2.8) is supported by the constraint equations, since $\frac{1}{\gamma}[\![\boldsymbol{u}]\!] \otimes^s \boldsymbol{n}_\Gamma = \boldsymbol{\mathcal{E}}^M$ allows for a constant jump between all node pairs that are on opposite sides of the discontinuity. It is important to note that the normal $\boldsymbol{n}_\Gamma$ and the macroscopic jump $[\![\boldsymbol{u}]\!]$ can point in different directions, depending on the mode of localization.

3.1.4. Homogenization

The same intuitive definition of the homogenized stress Eq. (2.16) as the volume averaged stress tensor is used. An analytical proof of satisfaction of the Hill-Mandel condition is not provided. However, it will be demonstrated with numerical examples in the next sections that the response is exactly the same as with the square RVE. Therefore, it can be assumed that energy equivalence is satisfied.

3.2. Implementation and algorithmic aspects

In this section, an overview is given of the implementation details required to impose the macroscopic strain via the periodic BCs (Eq. (3.17)) on a circular domain and subsequently extracting the homogenized response.

Central to the proposed framework is that the (unknown) microscopic jump $[\![\boldsymbol{u}]\!]$ in Eq. (3.17) is defined as the relative displacement between two nodes $\{\hat{\boldsymbol{x}}^-, \hat{\boldsymbol{x}}^+\}$ on the boundary that are closest to where the microscopic discontinuity crosses the edge (see Fig. 3.2). These nodes are denoted in the following as *opening nodes*. Note that with this approach, the selection of the *opening nodes* does not affect the response before localization when the jump is zero. Although outside the scope of this thesis, this feature allows for extending the framework such that the selection of *opening nodes* is determined on the fly when the RVE starts to localize, without convergence issues due to sudden changes in BCs.

In addition, the microscopic crack normal $\boldsymbol{n}_\Gamma$ in Eq. (3.17) is replaced by the macroscopic crack normal $\boldsymbol{n}_\Gamma^M$ such that the deformation after localization is consistent on both scales. The constrained equations in Eq. (3.17) can be expanded in matrix-vector format, resulting in

$$\begin{bmatrix} u_x^+ \\ u_y^+ \end{bmatrix} = \begin{bmatrix} u_x^- \\ u_y^- \end{bmatrix} + \left(\begin{bmatrix} \mathcal{E}_{xx}^M & \mathcal{E}_{xy}^M \\ \mathcal{E}_{xy}^M & \mathcal{E}_{yy}^M \end{bmatrix} - \frac{1}{\gamma} \begin{bmatrix} [\![u]\!]_x n_{\Gamma_x}^M & \frac{1}{2}([\![u]\!]_x n_{\Gamma_y}^M + [\![u]\!]_y n_{\Gamma_x}^M) \\ \frac{1}{2}([\![u]\!]_x n_{\Gamma_y}^M + [\![u]\!]_y n_{\Gamma_x}^M) & [\![u]\!]_y n_{\Gamma_y}^M \end{bmatrix} \right) \cdot \begin{bmatrix} x^+ - x^- \\ y^+ - y^- \end{bmatrix} + \begin{bmatrix} [\![u]\!]_x \\ [\![u]\!]_y \end{bmatrix} \tag{3.18}$$

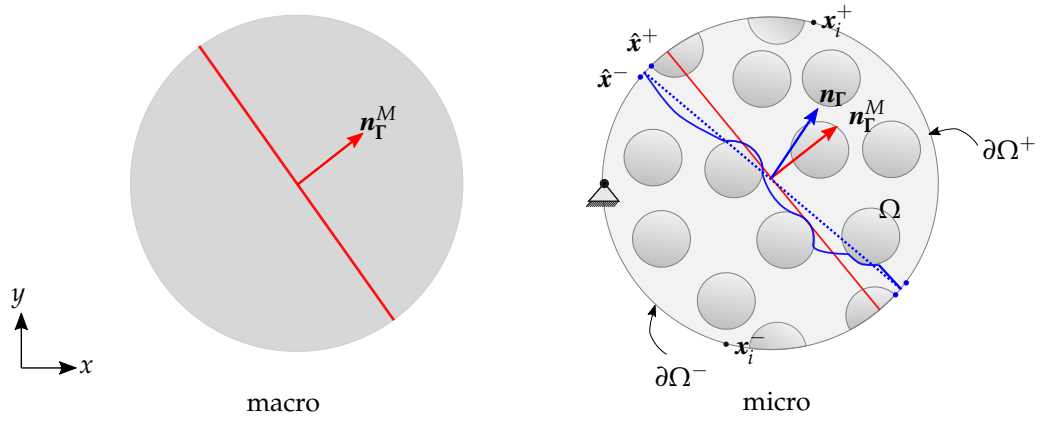

Figure 3.2: Schematic of the circular RVE with the nomenclature used for imposing the *mod*-PBCs.

The displacements in x-direction can be rewritten as

$$u_x^+ = u_x^- + \mathcal{E}_{xx}^M \Delta x + \mathcal{E}_{xy}^M \Delta y - \frac{1}{\gamma}([\![u]\!]_x n_{\Gamma_x}^M \Delta x + \frac{1}{2}([\![u]\!]_x n_{\Gamma_y}^M + [\![u]\!]_y n_{\Gamma_x}^M)\Delta y) + [\![u]\!]_x \tag{3.19}$$

where $\Delta x = x^+ - x^-$ and $\Delta y = y^+ - y^-$. Since the jump is defined as the relative displacement between the *opening nodes*, this can be expressed as

$$u_x^+ = u_x^- + \mathcal{E}_{xx}^M \Delta x + \mathcal{E}_{xy}^M \Delta y - \frac{1}{\gamma}(\hat{u}_x^+ - \hat{u}_x^-) n_{\Gamma_x}^M \Delta x - \frac{1}{2\gamma}(\hat{u}_x^+ - \hat{u}_x^-) n_{\Gamma_y}^M \Delta x + \frac{1}{2\gamma}(\hat{u}_y^+ - \hat{u}_y^-) n_{\Gamma_x}^M \Delta y + (\hat{u}_x^+ - \hat{u}_x^-) \tag{3.20}$$

Rewriting and collecting all coefficients per degree of freedom (DOF), results in

$$\begin{aligned} u_x^+ = u_x^- &+ \underbrace{\frac{1}{2\gamma}(-2n_{\Gamma_x}^M \Delta x - n_{\Gamma_y}^M \Delta y + 2\gamma)}_{Ax}\, \hat{u}_x^+ + \underbrace{\frac{1}{2\gamma}(2n_{\Gamma_x}^M \Delta x + n_{\Gamma_y}^M \Delta y - 2\gamma)}_{Bx}\, \hat{u}_x^- \\ &+ \underbrace{\frac{1}{2\gamma}(-n_{\Gamma_x}^M \Delta y)}_{Cx}\, \hat{u}_y^+ + \underbrace{\frac{1}{2\gamma}(n_{\Gamma_x}^M \Delta y)}_{Dx}\, \hat{u}_y^- + (\mathcal{E}_{xx}^M \Delta x + \mathcal{E}_{xy}^M \Delta y) \end{aligned} \tag{3.21}$$

The same can be done with the DOFs in y-direction, which yields

$$\begin{aligned} u_y^+ = u_y^- &+ \underbrace{\frac{1}{2\gamma}(-n_{\Gamma_y}^M \Delta x)}_{Ay}\, \hat{u}_x^+ + \underbrace{\frac{1}{2\gamma}(n_{\Gamma_y}^M \Delta x)}_{By}\, \hat{u}_x^- \\ &+ \underbrace{\frac{1}{2\gamma}(-n_{\Gamma_x} \Delta x - 2n_{\Gamma_y}^M \Delta y + 2\gamma)}_{Cy}\, \hat{u}_y^+ + \underbrace{\frac{1}{2\gamma}(n_{\Gamma_x}^M \Delta x + 2n_{\Gamma_y}^M \Delta y - 2\gamma)}_{Dy}\, \hat{u}_y^- + (\mathcal{E}_{xy}^M \Delta x + \mathcal{E}_{yy}^M \Delta y) \end{aligned} \tag{3.22}$$

3.2.1. Global description of the framework

The application of the constraint equations Eq. (3.21) and Eq. (3.22) is discussed in further detail in this section. An overview of the flow of actions described in the following is given in the form of pseudocode in Box 1 and a schematic of the used nomenclature is presented in Fig. 3.2.

Box 1 Applying the *mod*-PBCs and homogenizing the response on the circular RVE

Preparation

1: $\mathscr{M}, \mathscr{P}, \boldsymbol{n}_\Gamma^M \leftarrow$ readInput(f_{input}) - *read mesh, properties and macro norm from input file*
2: $\mathscr{B} \leftarrow$ detectBoundaryNodes($\mathscr{M}$) - *identify nodes that are on the edge of the RVE*
3: $\mathscr{B}^p \leftarrow$ makeBoundaryPairs($\mathscr{B}$) - *find node pairs of opposing nodes*

Start time step t

4: $\boldsymbol{\varepsilon}^M \leftarrow$ updateImposedStrain($\dot{\boldsymbol{\mathcal{E}}}^M$) - *compute new macroscopic strain at time t*
5: $\{\hat{\boldsymbol{x}}^+, \hat{\boldsymbol{x}}^-\} \leftarrow$ getOpeningNodes($\mathscr{B}$, $\boldsymbol{n}_\Gamma^M$) - *get nodes allocated to matrix material that are allowed to open*
6: $n_\Gamma \leftarrow$ updateMicroCrackNorm($\{\hat{\boldsymbol{x}}^+, \hat{\boldsymbol{x}}^-\}$) - *update micro crack normal*
7: $\{\mathscr{B}^+, \mathscr{B}^-\} \leftarrow$ sortBoundaryNodes($\mathscr{B}^p$, $\boldsymbol{n}_\Gamma$) - *sort boundary nodes, based on their side w.r.t. the discontinuity*
8: $\mathscr{C} \leftarrow$ fixSupport($\mathscr{B}$) - *remove rigid body translations*
9: $\mathscr{C} \leftarrow$ setModPBCs($\mathscr{B}^+$, $\mathscr{B}^-$, $\{\hat{\boldsymbol{x}}^+, \hat{\boldsymbol{x}}^-\}$, $\boldsymbol{\mathcal{E}}^M$) - *set modified periodic boundary conditions Eq. (3.17)*

Solve micro BVP at time t

After converged time step, do:

10: $\boldsymbol{\sigma}^{\boldsymbol{M}} \leftarrow$ computeMacroStress($\boldsymbol{u}$) - *compute macro stress tensor Eq. (2.16)*
11: $f_{output} \leftarrow$ writeStressStrain($\boldsymbol{\sigma}^M$, $\boldsymbol{\mathcal{E}}^M$) - *append stress-strain ouput data*

Go to next time step $t + \Delta t$ ...

After reading the mesh $\mathscr{M}$ and properties $\mathscr{P}$ (containing the material parameters, solver settings *etc*) from an input file f_{input}, the nodes on the boundary of the specimen $\mathscr{B}$ are detected with DETECTBOUNDARYNODES.

Subsequently, the procedure MAKEBOUNDARYPAIRS identifies opposing node pairs $\mathscr{B}^p$ with anti-periodic normals.

At each new time step t, the new macroscopic strain $\boldsymbol{\mathcal{E}}^M$ is updated through time integration with UPDATEIMPOSEDSTRAIN. Next, the *opening nodes* are determined with the procedure GETOPENINGNODES, based on the macroscopic jump normal vector $\boldsymbol{n}_\Gamma^M$ that is provided as an input and assumed to be *a priori* known.[2] In this approach, nodes $\boldsymbol{x}_i$ on the boundary which have the smallest dot-product with the macroscopic normal $(\boldsymbol{x}_i \cdot \boldsymbol{n}_\Gamma^M)$ are selected as *opening nodes* $\{\hat{\boldsymbol{x}}^-, \hat{\boldsymbol{x}}^+\}$, with the extra requirement that these nodes must be on the matrix side.[3]

When these *opening nodes* are identified, the microscopic crack normal $\boldsymbol{n}_\Gamma$ is defined as the vector that is orthogonal to the average relative coordinate vector between the *opening nodes* $\boldsymbol{n}_\Gamma := (\frac{1}{2}(\hat{\boldsymbol{x}}^- + \hat{\boldsymbol{x}}^+) - \boldsymbol{x}_c) \times \boldsymbol{e}_z$, where $\boldsymbol{x}_c$ is the center coordinate vector of the circular RVE and $\boldsymbol{e}_z$ is the basis vector that is aligned with the z-coordinate direction. Subsequently, it is checked if the normal is in the same direction as the macro crack normal $\boldsymbol{n}_\Gamma^M$. If this is not the case, then the direction is flipped $\boldsymbol{n}_\Gamma := -\boldsymbol{n}_\Gamma$. These steps are performed in UPDATEMICROCRACKNORM.

This microscopic crack normal $\boldsymbol{n}_\Gamma$ is subsequently used in SORTBOUNDARYNODES to identify which nodes are on the positive side (positive dot-product with microscopic crack normal) and which are on the negative side of the boundary (negative dot-product with microscopic crack normal) and stored in $\mathscr{B}^+$ and $\mathscr{B}^-$ respectively. Note that when inclusions are on the boundary of the RVE, $\boldsymbol{n}_\Gamma$ can point in a slightly different direction than the macroscopic normal $\boldsymbol{n}_\Gamma^M$.

Next, the BCs are imposed by updating the constraint object $\mathscr{C}$ with the procedures FIXSUPPORT and SETMODPBCs. This constraints object is subsequently used in solving the nonlinear microscopic BVP.

After solving at a certain time step t, the homogenized stress tensor $\boldsymbol{\sigma}^{\boldsymbol{M}}$ is computed with the line integral over the boundary of the specimen Eq. (2.16) in COMPUTEMACROSTRESS. The stress-strain data is then stored and after the full simulation is carried out, it is written to an output file f_{output} with WRITESTRESSSTRAIN.

Some more details on the procedure SETMODPBCs is provided in the next section.

3.2.2. Procedure for setting the modified PBCs

The procedure SETMODPBCs imposes the constraint equations Eq. (3.17) on the circular RVE. In terms of components in x and y direction (see Eq. (3.21) and Eq. (3.22)), the terms can be collected in the following containers, storing the master ($\mathcal{M}$) and slave ($\mathcal{S}$) degrees of freedom (DOFs), the corresponding coefficients ($\mathcal{C}$) and the inhomogeneous parts of the constraint equations ($\mathcal{R}$):

[2] When the micromodel is embedded in a multiscale FE^2 framework, the macro jump direction can be obtained with the acoustic tensor on the fly.

[3] Since fiber fracture is highly unlikely.

$$\mathcal{S} := \begin{bmatrix} u_x^+ \\ u_y^+ \end{bmatrix} \tag{3.23}$$

$$\mathcal{R} := \begin{bmatrix} \mathcal{E}_{xx}^M \Delta x + \mathcal{E}_{xy}^M \Delta y \\ \mathcal{E}_{xy}^M \Delta x + \mathcal{E}_{yy}^M \Delta y \end{bmatrix} \tag{3.24}$$

$$\mathcal{C} := \begin{bmatrix} 1 & Ax & Bx & Cx & Dx \\ 1 & Ay & By & Cy & Dy \end{bmatrix} \tag{3.25}$$

$$\mathcal{M} := \begin{bmatrix} u_x^- & \hat{u}_x^+ & \hat{u}_x^- & \hat{u}_y^+ & \hat{u}_y^- \\ u_y^- & \hat{u}_x^+ & \hat{u}_x^- & \hat{u}_y^+ & \hat{u}_y^- \end{bmatrix} \tag{3.26}$$

where

$$Ax = \frac{1}{2\gamma}(-2n_{\Gamma_x}^M \Delta x - n_{\Gamma_y}^M \Delta y + 2\gamma) \qquad Ay = \frac{1}{2\gamma}(-n_{\Gamma_y}^M \Delta x) \tag{3.27a}$$

$$Bx = \frac{1}{2\gamma}(2n_{\Gamma_x}^M \Delta x + n_{\Gamma_y}^M \Delta y - 2\gamma) \qquad By = \frac{1}{2\gamma}(n_{\Gamma_y}^M \Delta x) \tag{3.27b}$$

$$Cx = \frac{1}{2\gamma}(-n_{\Gamma_x}^M \Delta y) \qquad Cy = \frac{1}{2\gamma}(-n_{\Gamma_x} \Delta x - 2n_{\Gamma_y}^M \Delta y + 2\gamma) \tag{3.27c}$$

$$Dx = \frac{1}{2\gamma}(n_{\Gamma_x}^M \Delta y) \qquad Dy = \frac{1}{2\gamma}(n_{\Gamma_x}^M \Delta x + 2n_{\Gamma_y}^M \Delta y - 2\gamma) \tag{3.27d}$$

The containers are provided as arguments to the function ADDCONSTRAINT$(\mathcal{S}, \mathcal{R}, \mathcal{C}, \mathcal{M})$ in Jive, which subsequently adds the constraint equations to the constraints object $\mathscr{C}$. However, a special case must be handled when a node of a node pair on the positive side $\boldsymbol{x}^+$ is also an *opening node* $\hat{\boldsymbol{x}}^+$. In this case, it is both a slave and a master node. As Jive does not accept DOFs appearing on both sides of the constraint equations as both slave and master DOFs, a special case must be handled. For this case, the constraint equation can still be imposed unaffectedly by performing the steps described in Box 2

Box 2 Handling special case

1: Move DOF of master node $\boldsymbol{x}^-$ to the LHS, *i.e.* change master DOF to slave DOF and consequently
2: Change the sign of the RHS coefficients.
3: Move DOF of slave node $\boldsymbol{x}^+$ to RHS, *i.e.* change the coefficient of this DOF.
4: Since DOF of $\boldsymbol{x}^-$ is now on the LHS and the DOF of $\boldsymbol{x}^+$ is already an *opening node*, one coefficient is not needed anymore. Therefore the containers reduce in size by one column.

Performing the steps described in Box 2, the containers change to

$$\mathcal{S} := \begin{bmatrix} u_x^- \\ u_y^- \end{bmatrix} \tag{3.28}$$

$$\mathcal{R} := \begin{bmatrix} -(\mathcal{E}_{xx}^M \Delta x + \mathcal{E}_{xy}^M \Delta y) \\ -(\mathcal{E}_{xy}^M \Delta x + \mathcal{E}_{yy}^M \Delta y) \end{bmatrix} \tag{3.29}$$

$$\mathcal{C} := \begin{bmatrix} (1-Ax) & -Bx & -Cx & -Dx \\ -Ay & -By & (1-Cy) & -Dy \end{bmatrix} \tag{3.30}$$

$$\mathcal{M} := \begin{bmatrix} \hat{u}_x^+ & \hat{u}_x^- & \hat{u}_y^+ & \hat{u}_y^- \\ \hat{u}_x^+ & \hat{u}_x^- & \hat{u}_y^+ & \hat{u}_y^- \end{bmatrix} \tag{3.31}$$

which are added to the constraints object via ADDCONSTRAINT($\mathcal{S}$,$\mathcal{R}$,$\mathcal{C}$,$\mathcal{M}$).

3.3. Concluding remarks

In this section, a new formulation is presented where the spurious over-constraining effect as observed in Sec. 2.5 with the original formulation is removed. This is achieved by adding an unknown jump term to the original periodic BCs, which is defined as the relative displacement of two nodes on the boundary of the RVE. The construction of the new formulation is such that the possibility of a full localization band is handled naturally, since the formulation reduces to the *std*-PBCs before localization and allows for a realistic failure mode after localization. The new *mod*-PBCs imply periodicity of the *smooth* microfluctuations originating from the heterogeneities, while the *sharp* part due to localization is free. This enables the possibility of a jump along the circular RVE boundary, which would otherwise be suppressed. In the next Chapter, the methodology is presented for verifying the formulation and testing the performance in terms of providing an isotropic response.

4

Methodology

This section discusses the approach that is used to assess the performance of the proposed formulation in providing an independent response with respect to the load orientation, which is the main objective of this thesis. In addition, details on the material models and the RVEs are given.

4.1. Assessing orientation dependence

In order to study and quantify the ability of the micromodels to provide an isotropic response, an equivalent macroscopic (constant) strain rate $\dot{\boldsymbol{\varepsilon}}^M$, as defined in Eq. (3.3), is applied on the RVEs. The components of $\dot{\boldsymbol{\varepsilon}}^M$ are in terms of a local coordinate system, which is rotated under 20 varying orientation angles $\theta(^\circ) \in \{0,5,...,90\}$ with respect to the global coordinate system (see Fig. 4.1).

The orientation dependence is assessed for two different cases, where the strain paths and material models are chosen such that the first case describes mode-I (opening) failure and the second case describes mode-II (sliding) failure (see Fig. 4.2), denoted as **load case A** and **load case B** respectively. The load cases and the constitutive laws are summarized in Tab. 4.1. The details of the material models are elaborated in Sec. 4.4.

Since the modes of deformation are *a priori* known, the microscopic crack normal vector $\boldsymbol{n}_\Gamma^M$ can be provided in order to determine the *opening nodes* on the circular RVE (see Sec. 3.2). In load case

Load case	Deformation	Imposed macro strain $\bar{\boldsymbol{\varepsilon}}^M$	Equivalent strain $\tilde{\varepsilon}$	Localization mode
A	Uniaxial tension	$\begin{bmatrix} \dot{\mathcal{E}}^M_{\tilde{x}\tilde{x}} & 0 \\ 0 & 0 \end{bmatrix}$	*Mazars*	Mode-I (opening)
B	Pure shear	$\begin{bmatrix} 0 & \dot{\mathcal{E}}^M_{\tilde{x}\tilde{y}} \\ \dot{\mathcal{E}}^M_{\tilde{x}\tilde{y}} & 0 \end{bmatrix}$	*von Mises*	Mode-II (sliding)

Table 4.1: Load cases and constitutive models.

Figure 4.1: Local $\bar{x},\bar{y}$-coordinate system rotated with angle θ with respect to a global x,y-coordinate systems of the square and circular RVE.

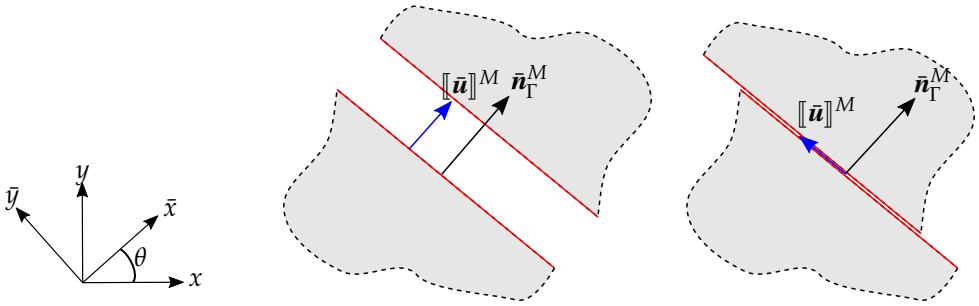

Figure 4.2: Macroscopic kinematics after localization. Left: mode-I localization. Right: mode-II localization. When the macroscopic bulk strain is zero, the equivalent macroscopic strain is $\bar{\boldsymbol{\varepsilon}}^M = \frac{|\Gamma|}{|\Omega|}[\![\bar{\boldsymbol{u}}]\!] \otimes^s \bar{\boldsymbol{n}}_\Gamma^M$. Note that in the case of mode-I localization $\mathcal{E}^M_{\bar{x}\bar{y}} = \mathcal{E}^M_{\bar{y}\bar{x}} = 0$, $\mathcal{E}^M_{\bar{x}\bar{x}} \neq 0$, $\mathcal{E}^M_{\bar{y}\bar{y}} = 0$ and in the case of of mode-II localization $\mathcal{E}^M_{\bar{x}\bar{y}} = \mathcal{E}^M_{\bar{y}\bar{x}} \neq 0$, $\mathcal{E}^M_{\bar{x}\bar{x}} = 0$, $\mathcal{E}^M_{\bar{y}\bar{y}} = 0$.

A, the normal always points in the direction of $\bar{x}$ (see Fig. 4.1). In load case B, there are two possible orientations for the shear band, with normal along $\bar{x}$ or along $\bar{y}$. In the current implementation of the *mod*-PBCs, without adaptive detection of the localization orientation, the *opening nodes* $\{\hat{\boldsymbol{x}}^-, \hat{\boldsymbol{x}}^+\}$ are selected to support a shear band with normal vector $\boldsymbol{n}_\Gamma^M$ in $\bar{x}$-direction.

For each orientation angle θ, the strain is rotated to the global x,y-coordinate system and applied on the RVEs. After solving the BVPs, the global stress-strain components are transformed to the local $\bar{x},\bar{y}$-coordinate system and used for comparing the response of the square and the circular RVEs.

4.2. Verification of the formulation

The new formulation of the *mod*-PBCs on the circular RVEs is verified by comparing the responses to those obtained with the well-established classical periodic BCs on square RVEs under load orientations resulting in single (supported) crack bands. For both load case A and B, this corresponds to loading orientation angles of $\theta = 0°$.

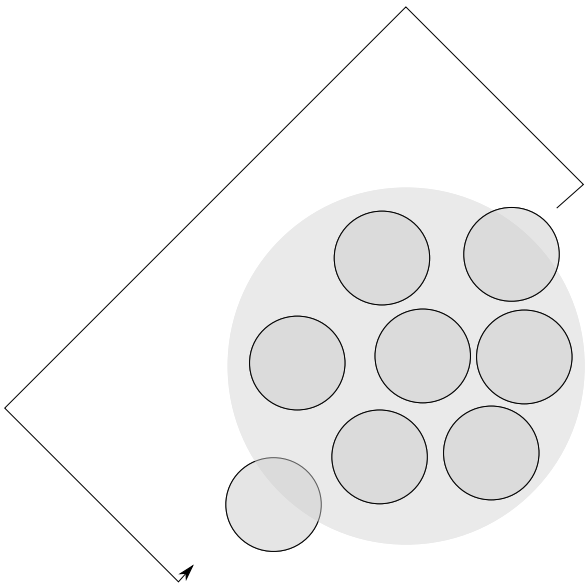

Figure 4.3: A circular RVE with periodic material. When an inclusion crosses the edge, a copy is mapped tot the opposite side.

4.3. Representative volume elements

4.3.1. Homogeneous RVE

A homogeneous RVE is considered in order to isolate the effect of the BCs and the RVE shape on the dependence of the response on the load orientation, since both the square and the circular RVE represent the same (homogeneous) microstructure, without any interference of *wall-effects*. In addition, the RVE size dependency after localization can be assessed, which is important in comparing RVEs with different shapes and consequently different sizes.

4.3.2. Heterogeneous RVE

As part of this thesis, a definition is presented for a circular heterogeneous RVE without *wall-effects* (see Fig. 4.3). This is achieved by allowing inclusions to cross the edge and letting exiting inclusions re-enter on the opposite sides, such that a mixed-coupling of matrix-inclusion between opposing points is prevented and that each node has an associated node on the opposite side. However, a slight overlap between exiting and re-appearing inclusions results in a larger contribution of these inclusions to the volume fraction, which is taken into account when generating circular RVEs.

Since heterogeneous RVEs, representing realistic random microstructures, should be independent of the loading orientation in an average sense, individual RVEs generally suffer from directional bias. As the RVE size increases and more inclusions are added to the domain, the scattering between individual realizations decreases and the response of a single realization can be considered as sufficiently representative. Therefore, a statistical study with uniaxial tension (load case A in Tab. 4.1) is performed with six distinct RVE sizes and 30 realizations each in order to study the convergence of effective properties with increasing RVE size and to determine a suitable RVE size. With the determined RVE size, the performance in providing an isotropic response can assessed.

4.3.3. RVE size dependence in softening

The well-known deterministic size effect [6], which also applies to the new formulation of the circular RVEs, is used in order to establish a consistent comparison between both RVE shapes with corresponding BCs. This is achieved by considering sizes of each shape such that the ratio of the (assumed) macroscopic crack length over the RVE volume (area in 2D with unit thickness) is consistent when comparing the circular RVE with the square RVE. It is recognized that this only allows for comparing the responses of both shapes and that no conclusions can be made on the actual responses, since the RVE does not exist in the softening regime. When the circular RVE is embedded in a multiscale framework for strain localization problems, then the (RVE size objective) traction-separation law (TSL) is the homogenized constitutive law after the RVE localizes, instead of the stress-strain relation. However, since this deterministic size effect is consistent and thus the dissipated energy is the same for both the square and the circular RVE, the volume averaged stress-strain curves as a result of classical first order computational homogenization, can still be compared. This approach allows for a single scale analysis, which is sufficient for the purpose of this thesis (Sec. 1.2), *i.e.* demonstrating that arbitrary localization angles are supported by the applied BCs and a physically realistic (softening) failure mode is supported.

4.4. Microscale material model

Although it is recognized that the interface between inclusions and matrix can have a large influence on the mechanical response of composites, this is not taken into account in these studies in favor of simplicity. Therefore, interfacial de-bonding is not modeled, thereby assuming a perfect bond between the matrix and the inclusions.

The heterogeneous micromodels that are considered consist of two material phases: matrix and random, circular-shaped, inclusions. The material model adopted for the inclusions is an isotropic linear elastic constitutive law while the matrix material is a mesh-size independent and fracture energy regularized isotropic continuum damage model (CDM) with linear softening (see Fig. 4.4).

In this model, it is assumed that the material stiffness decreases due to degradation processes in the microstructure. Apart from the difference in unloading, these continuum damage models are robust compared to other material models, like softening plasticity, since the (total) stresses can be directly computed from the (total) strains. This makes it a good candidate for the studies in this work. Well-known issues with mesh alignment resulting in mesh-conform localization bands are accepted and assumed to have little impact on the results and the derived conclusions.

In addition, the analyses are based on the small-strain assumption and a quasi-static loading, *i.e.* the equilibrium is considered in the undeformed configuration and the loading is considered to vary slowly, such that inertia effects can be ignored. Furthermore, simulations are performed in a two-dimensional plane strain condition.

4.4.1. Continuum damage model

In the sequel, a brief description of the continuum damage model is provided, according to [16].

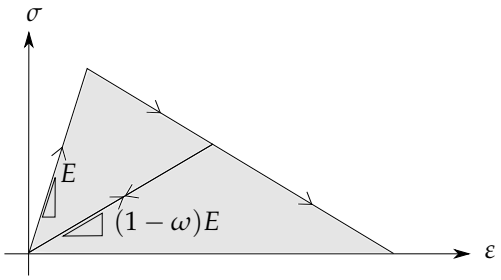

Figure 4.4: Bilinear damage model in 1D.

The (total) stress-strain relation can be expressed as

$$\boldsymbol{\sigma} = (1-\omega)\boldsymbol{D}_e : \boldsymbol{\varepsilon} \tag{4.1}$$

where $\boldsymbol{D}_e$ is the elastic stiffness matrix and ω is the damage parameter. The damage parameter is related to the history parameter κ, which keeps track of the highest equivalent strain $\tilde{\varepsilon}$ experienced by the material. A linear damage evolution law is used and can be described as

$$\omega(\kappa) = \begin{cases} 0 & \text{if } \kappa < \kappa_i \\ \frac{\kappa_u}{\kappa}\frac{\kappa-\kappa_i}{\kappa_u-\kappa_i} & \text{if } \kappa_i \leq \kappa < \kappa_u \\ 1 & \text{if } \kappa \geq \kappa_u \end{cases} \tag{4.2}$$

where $\omega = 0$ corresponds to no damage before the damage threshold κ_i and $\omega = 1$ corresponds to complete material failure at the ultimate value of κ_u. The equivalent strain measures for each load case in Tab. 4.1 are described in the next subsection.

4.4.2. Equivalent strain measures per load case

For studying mode-I localization as a result of uniaxial strain (**load case A** in Tab. 4.1), the *Mazars* equivalent strain measure is used to trigger crack opening, which is defined as

$$\tilde{\varepsilon} = \sqrt{\sum_{i=1}^{3} (<\varepsilon_i>)^2} \tag{4.3}$$

where ε_i are the principal strains with $<\varepsilon_i> = \varepsilon_i$ in the case of tension ($\varepsilon_i > 0$) and $<\varepsilon_i> = 0$ in the case of compression ($\varepsilon_i < 0$).

For studying mode-II localization, the *von Mises* equivalent strain measure is used to obtain shear bands (**load case B** in Tab. 4.1), defined as

$$\tilde{\varepsilon} = \frac{1}{2}\sqrt{\frac{12}{(1+\nu)^2} J_2^{\varepsilon}} \tag{4.4}$$

where J_2^{ε} is the second invariant of the deviatoric strain tensor. For a more elaborate explanation and the implementation details of the continuum damage model, the reader is referred to [16].

4.5. Spurious modes

During the process of this thesis, it is observed that in a few number of cases spurious modes occurred with large sized RVEs and a high number of inclusions. Since the results of these modes can not be trusted and used in the analyses, specific material properties are chosen such that all simulations converged with realistic responses. A brief overview of the observations and some details are reported in App. A. It is thought that this is related to the continuum damage model and therefore does not influence the conclusions from this investigation.

5

Homogeneous RVE

The purpose of this chapter is to test the new formulation on the circular RVE and compare the improved performance with respect to the original formulation in [9] and the square RVE with classical periodic BCs. A homogeneous RVE is considered in order to isolate the influence of the shape on the response. Moreover, a homogeneous microstructure can be represented by a (single) homogeneous RVE without considering *wall-effects* and statistical analyses. This allows for a consistent comparison between both RVE shapes.

5.1. Computational models

The circular RVE has a radius $R = 0.5$ mm and the square RVE has a height and width $h = w = 1$ mm. Since the material is homogeneous, localization can start anywhere in the domain, resulting in convergence issues since multiple solutions exist at the onset of softening. Due to roundoff errors and mesh-alignment sensitivity, localization will be triggered anywhere in the specimen. In order to avoid this and allow for a controlled localization that always runs through the middle, a small portion in the center of the specimen is perturbed by allocating a reduced fracture strength. The magnitude of the reduction is chosen to be 50%. A sensitivity study is performed from which it is concluded that the magnitude has very small effects on the response. The discretizations with three different mesh sizes are shown in Fig. 5.1. The darker area represents the area (radius $r = 0.025$ mm) with the reduced fracture strength to trigger localization. The material properties are given in Tab. 5.1.

Youngs' modulus E	Poisson's ratio ν	Tensile strength f_t	Fracture energy G_f
400 MPa	0.0 -	5 MPa	0.7 kJ/m^2

Table 5.1: Material properties of the homogenous RVEs.

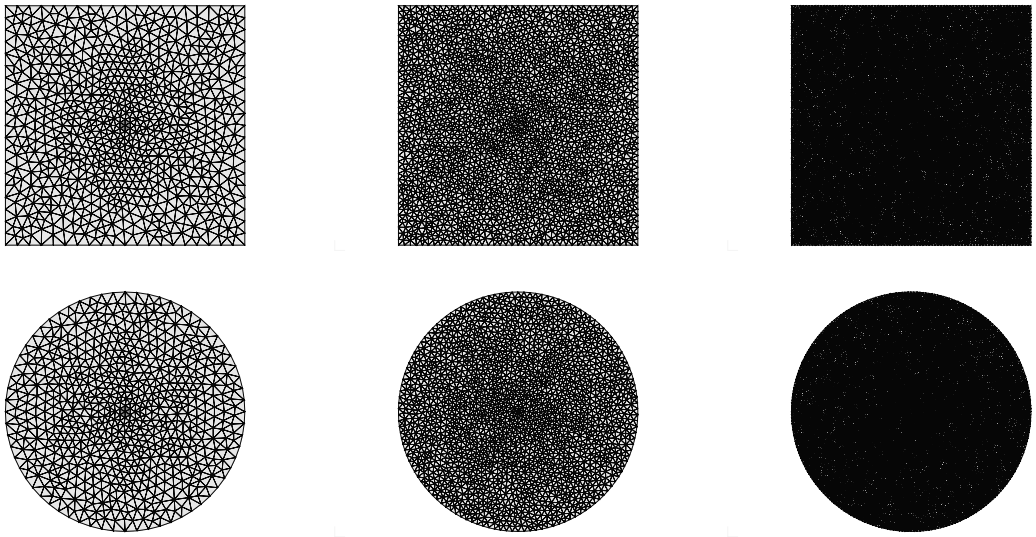

(a) Coarse (b) Medium (c) Fine

Figure 5.1: Discretisations with three distinct mesh sizes.

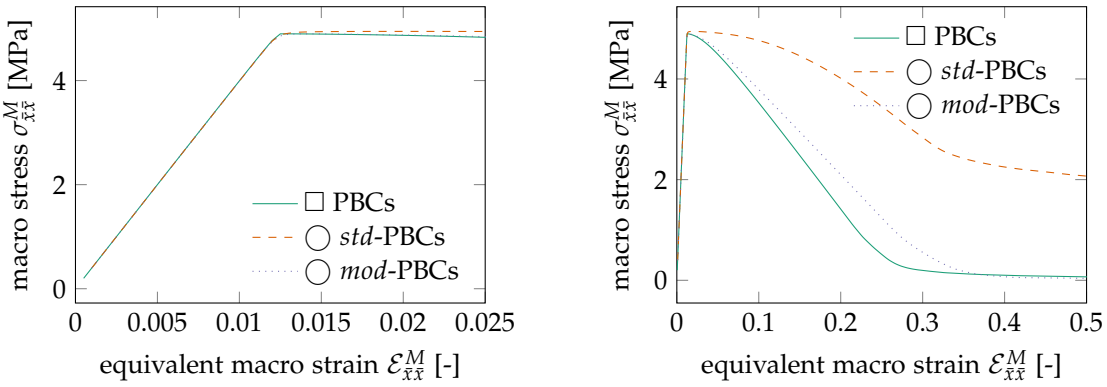

(a) Elastic response (b) Full response

Figure 5.2: Comparison of the response obtained with the three micromodels under horizontal uniaxial loading (load case A, $\theta = 0°$).

5.2. Verification

A mesh dependency study is performed where the square and circular RVEs are loaded with a uniaxial macroscopic strain (load case A) under orientation angle $\theta = 0^\circ$ (see Tab. 4.1).

The results are depicted in Fig. 5.3 from which it can be verified that the damage model, regularized with the fracture energy approach, is mesh-size independent. Moreover, the slight non-linearity in the stress-strain curves can be attributed to the imperfection and the mesh-orientation dependency of the continuum damage model.

It can be observed from Fig. 5.3 that all formulations, including the *mod*-PBCs, are mesh-size independent. This is expected since the micro jump in Eq. (3.17) is defined as the relative displacement vector between the nodes on the boundary where the crack localizes. With a fracture energy regularized CDM, the jump is smeared over the element. With larger elements, the jump is smeared over a larger area, while the overall magnitude is unchanged.

In addition, Fig. 5.2a shows that the square and the circular RVEs with both the *std*-PBCs and the *mod*-PBCs respectively, predict the same response in the elastic regime. This is in agreement with the expectations since the formulation of the *mod*-PBCs reduces to the *std*-PBCs prior to localization of the RVE.[1] In addition, the slope of the stress-strain curve corresponds to the Young's modulus $E = 400$ MPa (note that the Poisson's ratio is zero, thus $\sigma_{xx} = E\varepsilon_{xx}$).

For the rest of the studies in this chapter, the medium mesh is used (see Fig. 5.1).

5.3. Isotropy study: mode-I deformation

In this section, a uniaxial equivalent macro strain strain (load case A) is applied under varying orientation angles $\theta(^\circ) \in \{0,\ldots,90\}$ on both RVEs (see Tab. 4.1). The macroscopic axial stress component $\sigma^M_{\bar{x}\bar{x}}$ is chosen as the quantity that is monitored and presented in the form of stress-strain curves and stress-orientation curves.

5.3.1. Results

The development of the inclined crack bands under loading orientation angle $\theta = 25^\circ$ is shown in Fig. 5.6. It can be observed that multiple inclined (perodic) parallel crack bands appear in the square RVE as soon as the first (middle) crack band reaches the boundary. In addition, the circular RVE with *std*-PBCs is clearly over-constraining, since the boundaries of the RVE cannot crack and thus a smooth strain field is not obtained, while the *mod*-PBCs successfully demonstrate the development of a single dominant crack band.

The deformed square RVE can be virtually stacked in horizontal and vertical directions, since opposing edges have compatible displacement fields enforced by the periodic constraints. This virtual stacking is shown in Fig. 5.4 for the load orientation angles $\theta = 0^\circ$, 25° and 45° at equal macroscopic strain values. The figure illustrates the artificial crack closure in the microstructure near the edges of the RVE when $\theta = 25^\circ$, which has a stiffening effect on the overall response and prevents full softening.

[1] The micro jump in Eq. (3.17) is zero before localization occurs.

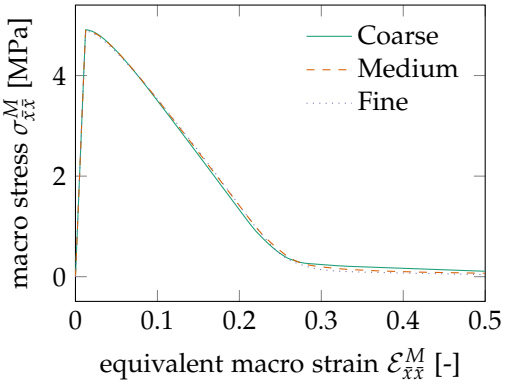

(a) Square RVE with periodic BCs

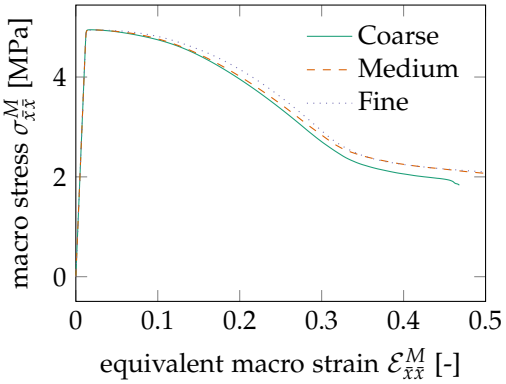

(b) Circular RVE with *std*-PBCs

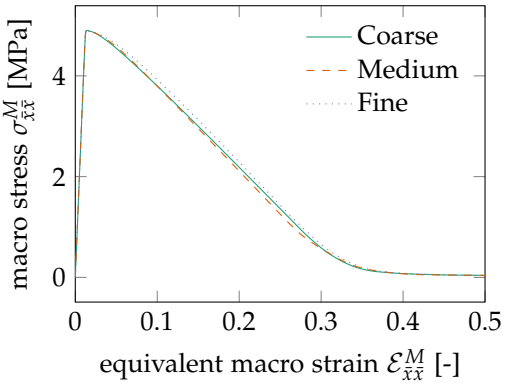

(c) Circular RVE with *mod*-PBCs

Figure 5.3: Stress-strain response from mesh (in)dependence study with load case A and orientation angle $\theta = 0°$.

Fig. 5.5 shows the results of the isotropy study with the circular and the square RVE. In this figure, the axial stress-strain is plotted for all orientation angles θ. At the peak and at a macroscopic equivalent strain of $\mathcal{E}^M_{\bar{x}\bar{x}} = 0.15$, the stress values are plotted in the stress versus orientation angle diagrams. It can be observed that for arbitrary angles, the square RVE exhibits a strong post-peak anisotropy, while the circular RVE provides an isotropic response with the *std*-PBCs and the *mod*-PBCs.

5.3.2. Discussion

The post-peak anisotropy observed with the square RVE is due to the periodic BCs which only allow periodic crack bands, resulting in single crack bands under $\theta = 0°$, $45°$ and $90°$ orientations or multiple parallel inclined crack bands. In addition, it can be observed that the post-peak anisotropy originates also from the shape of the RVE. That is, a crack band angle at $\theta = 45°$ is actually supported by the periodic BCs, resulting in a smooth strain field with a single localized crack band. However, the response is not the same as with the other supported angles at $\theta = 0°$ and $90°$. Therefore, square RVEs cannot represent a macroscopic (infinitesimal) material point of an (isotropic) homogeneous microstructure, due to their shape and finite size. Even with remedies to increase the number of supported crack band angles (aligned percolation path BCs [2] and aligned weakly periodic BCs

[24]), there is still a different post-peak response when the crack length varies (compare the response with $\theta = 0^\circ$ and $\theta = 45^\circ$ in Fig. 5.5b).[2]

Fig. 5.5 shows that the over-constraining effect with the original formulation is removed while at the same time the orientation independence, inherent to the circular shape, is maintained. The slight variation in stress-strain curves can be attributed to the mesh-alignment dependence originating from the local, fracture energy regularized, continuum damage model resulting in mesh-conform crack bands.

5.4. RVE size dependence study

The (in)objectivity of the stress-strain response with respect to the RVE size is studied where three circular RVE sizes with radii $R(\text{mm}) = \{0.5, 1.0, 2.0\}$ are considered and subjected to a unaxial strain (load case A) under an orientation angle $\theta = 0^\circ$ (see Tab. 4.1).

5.4.1. Results

The stress-strain curves obtained with the *mod*-PBCs applied to three distinct circular RVE sizes are presented in Fig. 5.7a. In addition, the dissipated energy, computed as the area under the homogenized stress-strain curve versus the ratio of the volume over the macroscopic crack length ($2R$), is shown in Fig. 5.7b.

5.4.2. Discussion

It can be observed from Fig. 5.7a that after the onset of macroscopic softening, the response is dependent on the RVE size. When the RVE size increases, the dissipated energy is inversely proportional to the ratio of the volume over the crack length $\gamma = \frac{|\Omega|}{|\Gamma|}$, as can be observed from Fig. 5.7b. Consequently, larger RVEs appear to have a more brittle response, which is a well-known consequence of classical homogenization [6]. This demonstrates that this scaling factor $\frac{|\Gamma|}{|\Omega|}$ is generic and does not relate to square domains only, but also to circular ones with the new *mod*-PBCs. Therefore, the square RVE has more area than the circular RVE with equal RVE heights, which results in more brittle stress-strain responses (compare Fig. 5.5a with Fig. 5.5c).

5.5. Isotropy study: mode-II deformation

In this section, mode-II localization is studied as a result of an equivalent macroscopic shear strain (load case B) under varying angles $\theta(^\circ) = \{0, ..., 90\}$ (see Tab. 4.1). For this purpose, the circular RVE with radius $R = 0.5$ mm is considered. The observation from the RVE size dependency study in the previous section is used, in order to compare the response of the new formulation on circular RVEs with the response of the square RVEs with classical periodic BCs. A square RVE with height and width $h = w = 0.75$ mm is used such that the ratio of crack length over the volume $\frac{|\Gamma|}{|\Omega|}$ is the same for both RVEs and the energy dissipation is equal.

[2] When crack bands are oriented with $\theta = 0^\circ$, 45° and 90°, the application of the aligned weakly periodic BCs is equivalent to the strong periodic BCs.

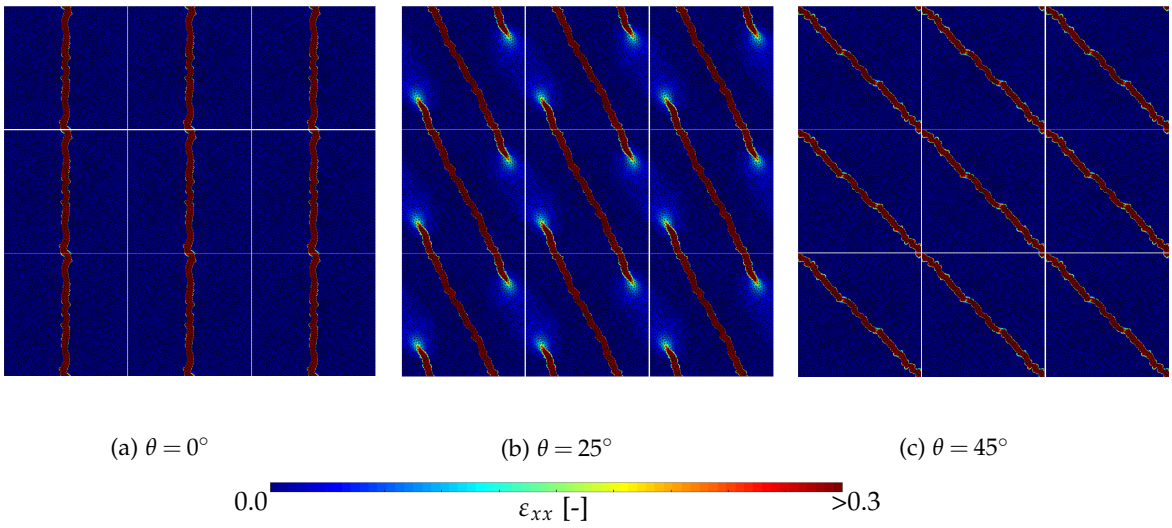

Figure 5.4: Stacked (undeformed) square RVEs with periodic BCs and contours of the microscopic strain field ε_{xx}.

5.5.1. Results

The development of the shear localization band is shown in Fig. 5.9 for both the square and the circular RVE with load orientation angle $\theta = 30°$. The final localization patterns as a result of five orientation angles θ are shown in Fig. 5.10 and the shear stress-strain curves for all orientation angles and both RVE shapes are presented in Fig. 5.8.

5.5.2. Discussion

As it can be observed, the sliding mode is supported by the proposed constraint equations Eq. (3.17) on a circular RVE and independent of the loading orientation angle θ, resulting in an isotropic response.

In the case when the macro jump $[\![\boldsymbol{u}]\!]^M$ vector is orthogonal to the localization band normal vector $\boldsymbol{n}_\Gamma^M$, a sliding mode is imposed on the RVE (see Fig. 4.2). In the limit case that the RVE is in a fully failed state, the macro bulk strain $\boldsymbol{\varepsilon}_b^M$ is zero and the equivalent macroscopic strain, as defined in Eq. (3.3), consists of only the macroscopic jump term $\frac{|\Gamma|}{|\Omega|}[\![\boldsymbol{u}]\!]^M \otimes^s \boldsymbol{n}_\Gamma^M$ with nonzero off-diagonal entries ($\mathcal{E}_{\bar{x}\bar{y}}^M = \mathcal{E}_{\bar{y}\bar{x}}^M \neq 0$, $\mathcal{E}_{\bar{x}\bar{x}}^M = 0$, $\mathcal{E}_{\bar{y}\bar{y}}^M = 0$). A fully failed state is supported by the *mod*-PBCs when $\frac{1}{\gamma}[\![\boldsymbol{u}]\!] \otimes^s \boldsymbol{n}_\Gamma = \boldsymbol{\mathcal{E}}^M$, where the constraint equations allow for a constant jump $\boldsymbol{u}^+ = \boldsymbol{u}^- + [\![\boldsymbol{u}]\!]$ between nodes on either side of the crack (see Eq. (3.17)). Therefore, $[\![\boldsymbol{u}]\!] \otimes^s \boldsymbol{n}_\Gamma = \gamma \boldsymbol{\mathcal{E}}^M = [\![\boldsymbol{u}]\!]^M \otimes^s \boldsymbol{n}_\Gamma^M$. Since the micro normal is (almost) equal to the macro normal $\boldsymbol{n}_\Gamma^{\boldsymbol{M}}$ (see Fig. 3.2) and since $\gamma = \frac{|\Omega|}{|\Gamma|}$, it follows that the macro jump is equal to the micro jump ($[\![\boldsymbol{u}]\!] = [\![\boldsymbol{u}]\!]^M$), which results in the sliding mode that is consistent with the deformation on the macroscale.

With the square RVE and periodic BCs, imposing the shear strain (Tab. 4.1) results in a failure mode where the sliding direction is not unique and can be in two orthogonal directions. This can be seen from Fig. 5.10 where the sliding direction for $\theta = 0°$ is in horizontal direction, whereas with the circular RVE it is in vertical direction. This is because the macroscopic crack normal $\boldsymbol{n}_\Gamma^M$ is *a priori* prescribed on the circular RVE for determining the *opening nodes*, which is not the case with the

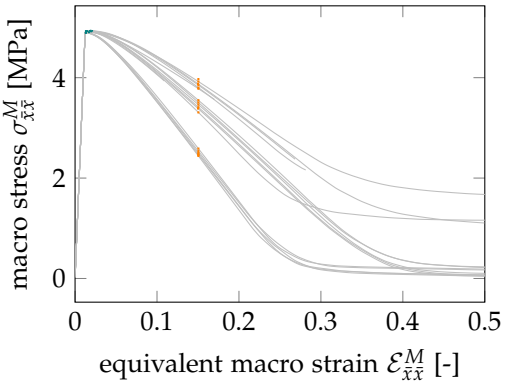

(a) Square RVE with periodic BCs

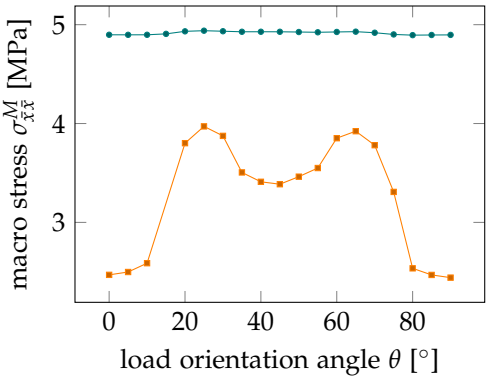

(b) Square RVE with periodic BCs

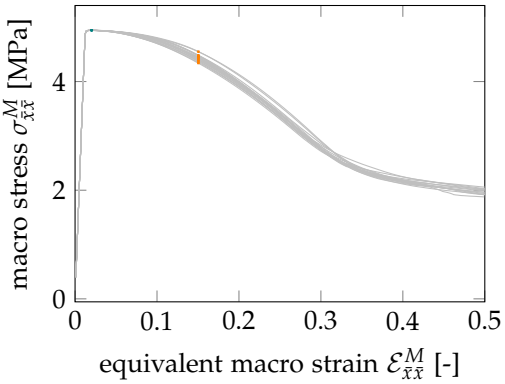

(c) Circular RVE with *std*-PBCs

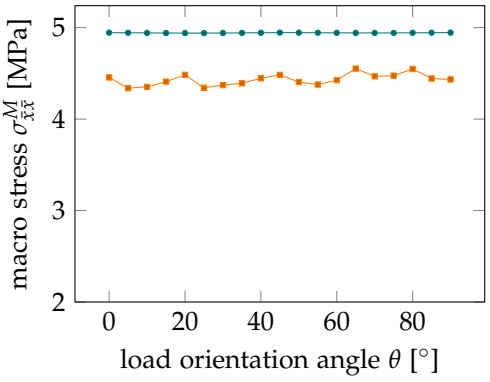

(d) Circular RVE with *std*-PBCs

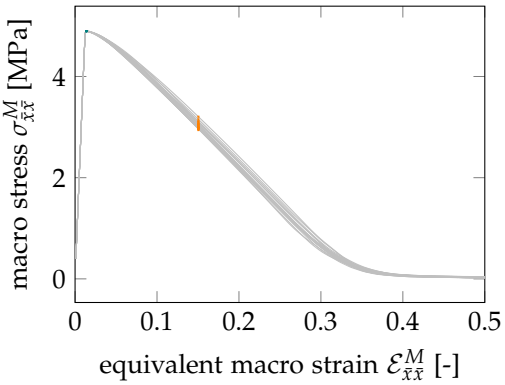

(e) Circular RVE with *mod*-PBCs

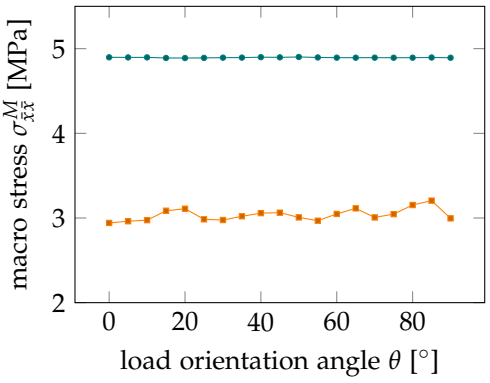

(f) Circular RVE with *mod*-PBCs

Figure 5.5: Stress-strain (left) and stress-orientation (right) curves corresponding to load case A.

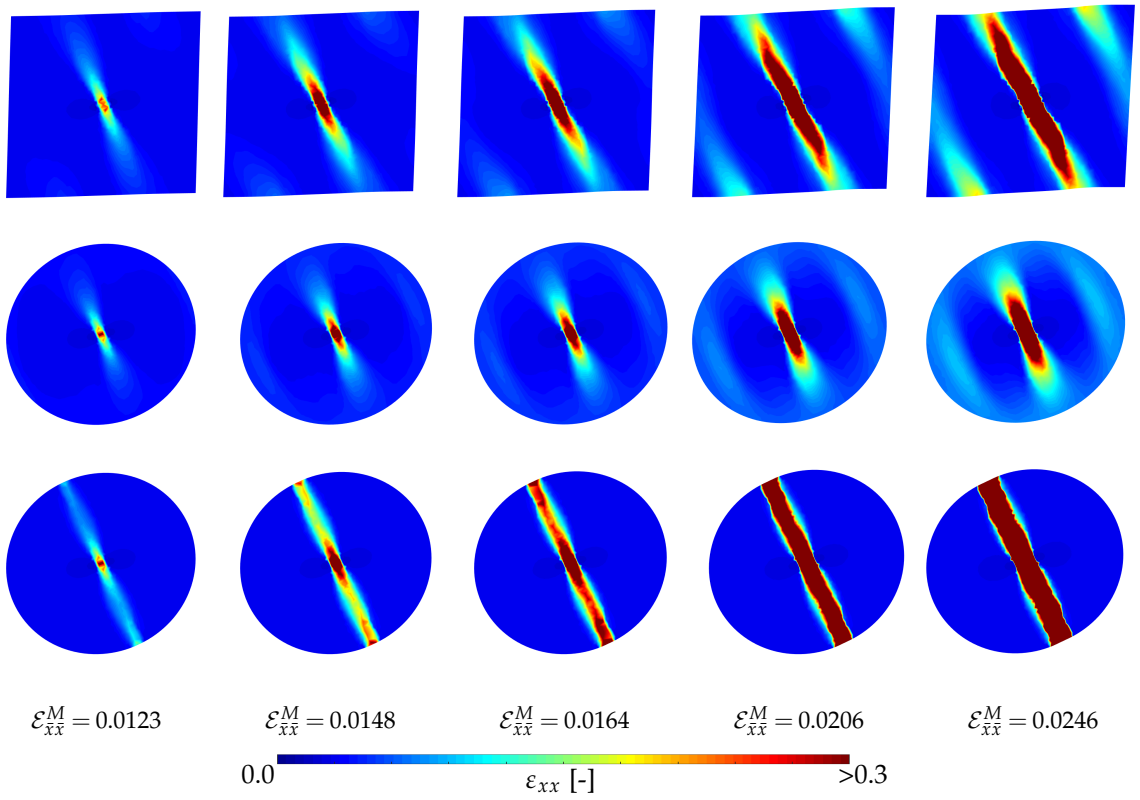

Figure 5.6: Development of localization (mode-I) as a result of load case A and orientation angle $\theta = 25°$ with contour plots of strain component ε^M_{xx} (deformation $x3.0$). Top: square RVE with periodic BCs. Middle: circular RVE with *std*-PBCs, Bottom: circular RVE with *mod*-PBCs.

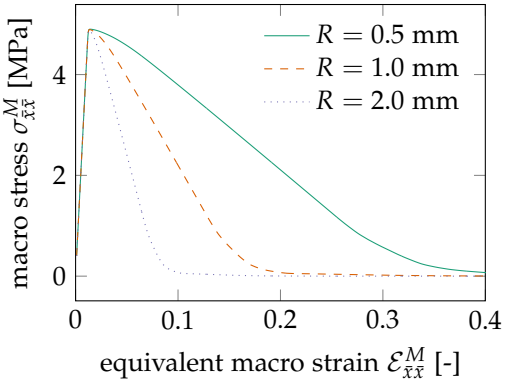

(a) Stress-strain curve obtained with three distinct circular RVE sizes

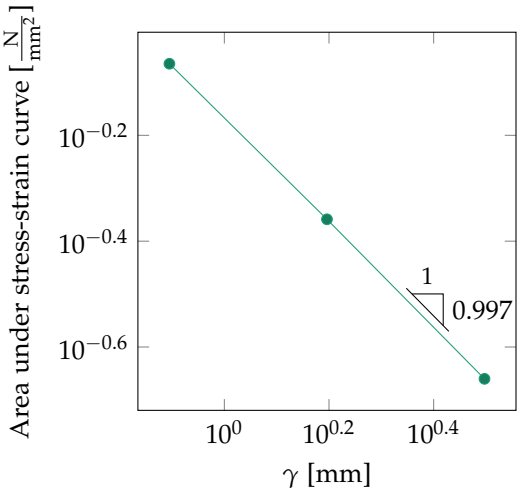

(b) Area under the stress strain curves versus ratio γ (area over crack length)

Figure 5.7: RVE size dependence study (load case A) with the circular RVE and *mod*-PBCs.

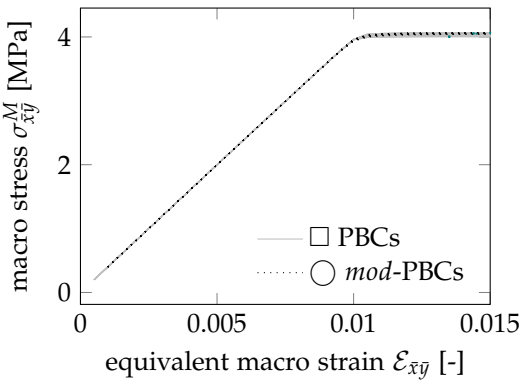

(a) Elastic response

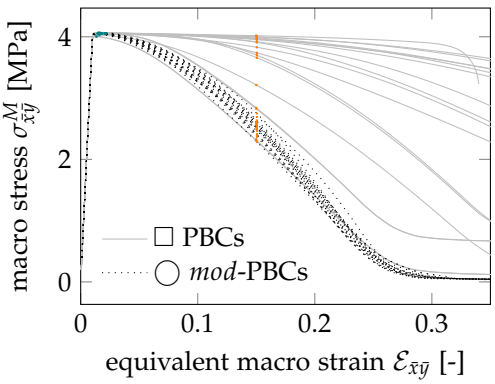

(b) Full response

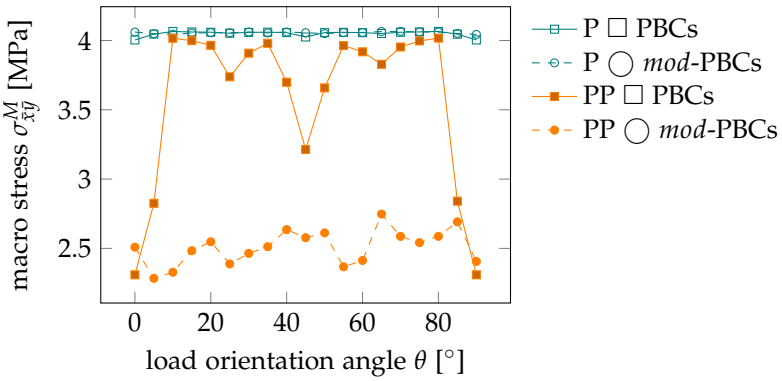

(c) Stress versus orientation angle θ. The peak (P) and post peak (PP) stress values in the stress-strain plots are plotted versus the orientation angle θ.

Figure 5.8: Isotropy study results with mode-II (sliding) as a result of load case B.

square RVE where two sliding modes, with orthogonal sliding directions, both satisfy the imposed shear deformation via the periodic BCs.

Furthermore, it can be concluded that also in the case of mode-II localization, the circular RVE with the *mod*-PBCs supports all sliding localization angles and provides an isotropic response, whereas the square RVE supports only $\theta = 0°$, $45°$ and $90°$ localization angles.

5.6. Concluding remarks

With the numerical examples that were performed in this chapter, it is demonstrated that the circular RVE with original *std*-PBCs does not perform well in a localization analysis, which is in agreement with the conclusions from the analytical example in Sec. 2.5.

Furthermore, the new formulation of *mod*-PBCs predicts the same response as the square RVE when the loading orientation leads to supported (single) localization band angles *and* provides a fully isotropic response with arbitrarily inclined angles. In addition, it is shown that the same RVE size dependence with classical (volume) homogenization [6] also applies to the circular RVE with the proposed formulation of the *mod*-PBCs. This explains the more brittle homogenized stress-strain

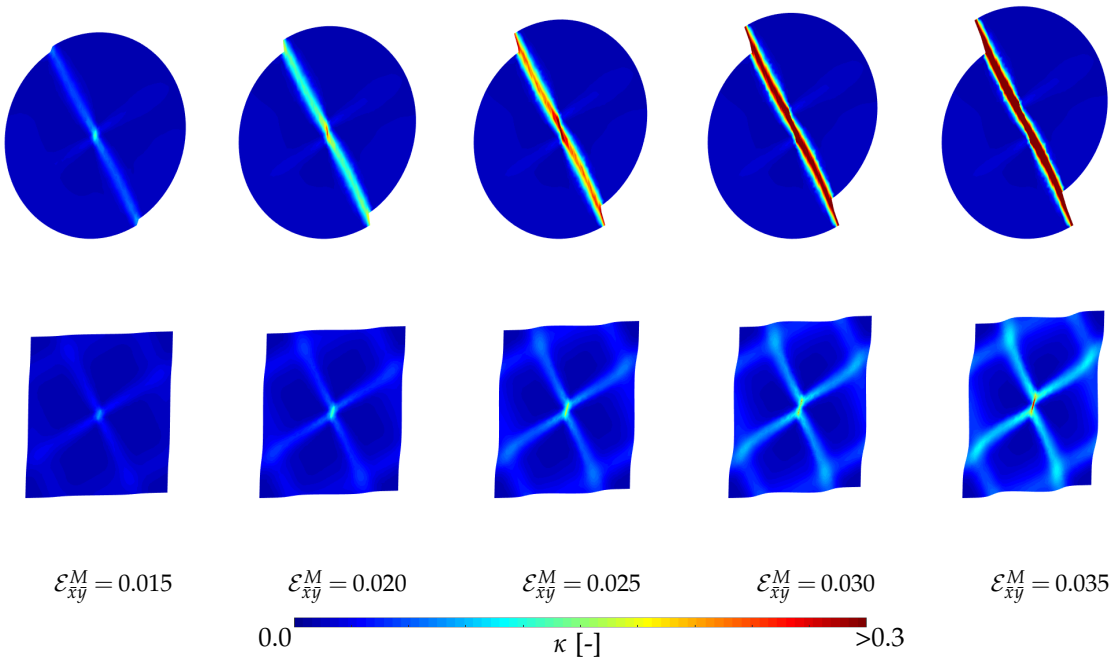

Figure 5.9: Development of localization (mode-II) as a result of load case B and orientation angle $\theta = 30°$ with contour plots of history variable κ (deformation x5.0).

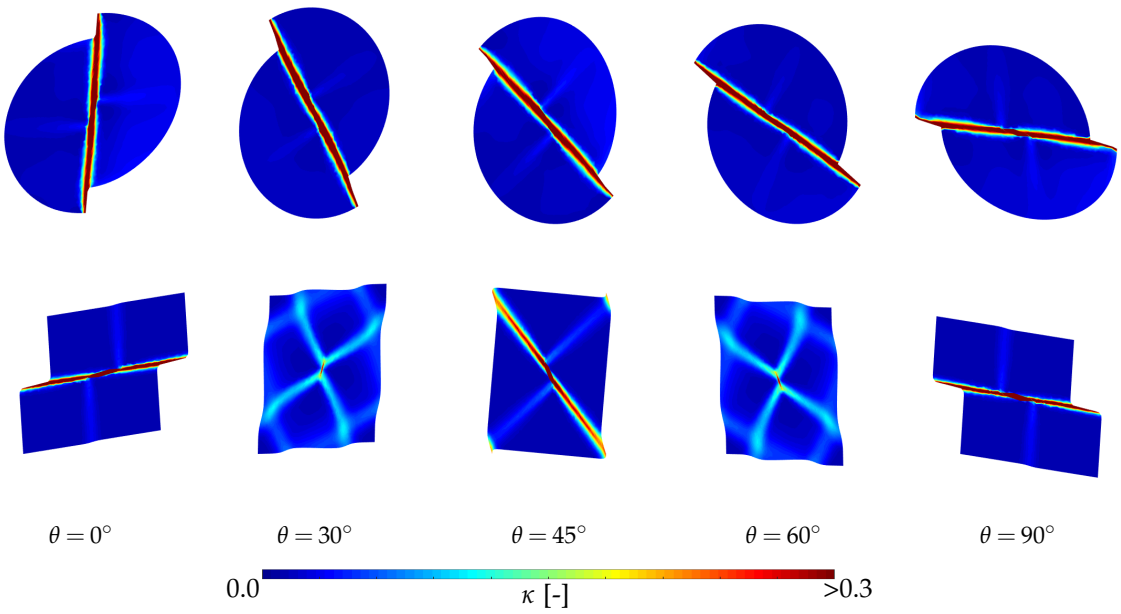

Figure 5.10: Deformed RVEs at $\mathcal{E}^M_{\bar{x}\bar{y}} = 0.035$ (deformation x5.0) with contours of history variable κ, as a result of load case B and five different orientation angles θ, describing mode-II (sliding) failure.

response with the circular RVE compared to the square RVE with equal heights.

6

Heterogeneous RVE

In this chapter, the performance of the *mod*-PBCs is tested with a circular heterogeneous RVE, representing a general two-phase random microstructure.

First, the ability of the new circular RVE in representing a random microstructure without *wall-effects* is explored (see Sec. 4.3.2). For comparison purposes, the well-established square RVE with classical periodic BCs and periodic material is used as a reference. Since the representativeness increases with the RVE size, a statistical analysis with six RVE sizes and 30 realizations per size is performed.

Based on the results of the statistical analysis, a proper RVE size is determined, which is used in assessing the independence of the response with respect to the loading orientation, which is the main focus of this thesis. Since the response of the RVE in softening depends on the size, the volume over the crack length ratio is used to establish a consistent comparison between both the circular and the square RVE.

6.1. Computional models

In order to keep the quality of the mesh, a maximum distance between inclusion edges is prescribed of 0.005 mm. The inclusions have a diameter of 0.1 mm and the volume fraction is chosen as $\rho = 0.5\%$. This choice is close to the maximum ratio that can be reached with the simple algorithm that is used

	Square						Circular					
Size	1	2	3	4	5	6	1	2	3	4	5	6
Height [mm]	0.561	0.868	1.12	1.40	1.68	1.97	0.640	0.954	1.27	1.59	1.91	2.22
Area [mm^2]	0.314	0.754	1.26	1.95	2.83	3.90	0.322	0.715	1.27	1.99	2.87	3.87

Table 6.1: Geometric properties of the RVEs.

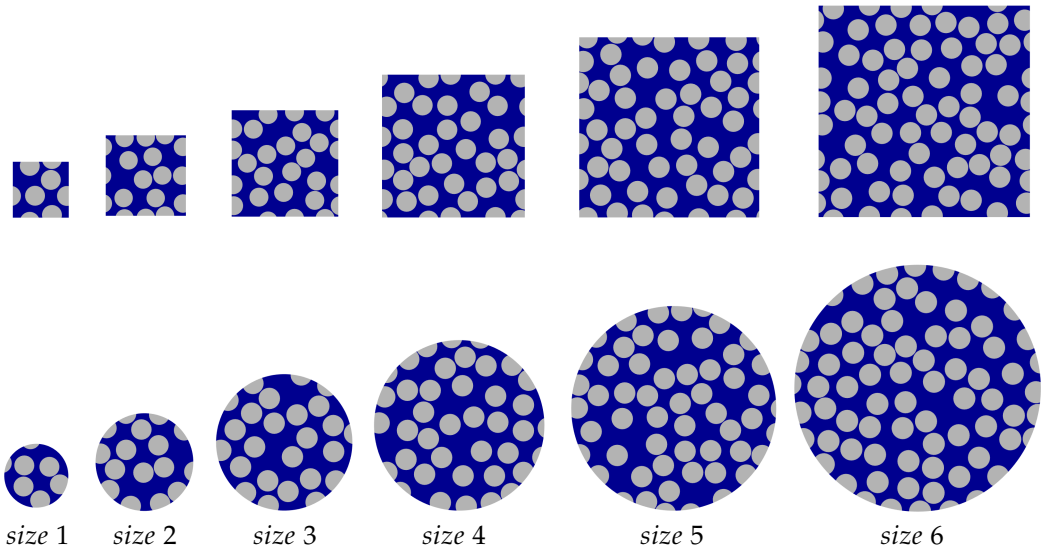

Figure 6.1: Heterogeneous RVE sizes.

Phase	Youngs' modulus E	Poisson's ratio ν	Tensile strength f_t	Fracture energy G_f
Inclusion	12970 MPa	0.46	-	-
Matrix	4000 MPa	0.15	50 MPa	10 kJ/m^2

Table 6.2: Material properties heterogeneous RVE.

in this study to obtain the circular RVEs. Material periodicity (as defined in this thesis in Sec. 4.3.2) for the circular micromodels results in a slight overlap of inclusions that exit the edge and re-appear on the other side. Therefore, these inclusions have slightly more area than the inclusions inside the domain that do not cross the edge. Consequently, different volume fractions can be obtained with the same number of inclusions in the RVE. This is not the case with the square RVE realizations, where the number of (periodic) inclusions determines the volume fraction for a fixed geometry. In order to keep the volume fraction constant for all realizations, the height of the square RVEs is determined from an integer number of inclusions and the volume fraction $\rho = 0.5\%$. Subsequently, circular RVEs sizes with approximately the same areas as the square RVEs are determined.[1] The geometric properties of the six RVE sizes shown in Fig. 6.1 are summarized in Tab. 6.1. Note that the *true* volume fraction can be slightly different for each realization, since the circular boundaries of both the RVE domain and the inclusions (and thus also the overlap) are discretized. However, with increase of RVE size, this effect diminishes.

The material properties are tabulated in Tab. 6.2. In all cases, the same discretization is used. The domain is discretized with constant strain triangular elements with single point Gauss integration rules. Furthermore, elements with a typical size of 0.02 mm are used.

[1]For certain combinations of circular RVE sizes and inclusion radii it required an extreme amount of iterations of generating RVEs to get the volume fractions within the specified tolerance. Therefore, slightly perturbed areas are chosen in order to generate RVEs within a reasonable amount of time. This explains the slight difference in area between both shapes and decimal values.

6.2. RVE size statistical study

In this study, the square and the circular RVEs with six sizes and 30 realizations are subjected to a constant uniaxial macroscopic strain (load case A) under orientation angle $\theta = 0^\circ$ (see Tab. 4.1).

The sample mean and standard deviations are computed as

$$\mu_x = \frac{1}{N}\sum_{i=1}^{N} x_i \tag{6.1}$$

$$\sigma_x = \sqrt{\frac{1}{N-1}\sum_{i=1}^{N}(x_i - \mu_x)^2} \tag{6.2}$$

where variable x denote the peak strain or peak stress.

6.2.1. Results

A typical stress-strain response from a single realization of the largest square and circular RVEs is depicted in Fig. 6.2. The stress-strain curves from all realizations of the smallest (*size* 1) and the largest (*size* 6) are presented in Fig. 6.4.

The results from the statistical analysis are shown in Fig. 6.3. Besides the observation that the responses are approximately equal and that the scatter in effective quantities are significantly reduced with large RVE sizes (as statistical representativeness increases), several other observations can be made:

- The standard deviation in the peak stress is consistently larger with the circular RVE compared to the square RVE.
- The circular RVEs tend to predict (slightly) higher peak stresses compared to the square RVEs.
- The maximum peak stress of the circular RVEs tends to occur at smaller macroscopic strain values compared to the square RVEs.

The crack band patterns after the peak stress of five RVEs with *size* 5 are shown in Fig. 6.5. This figure indicates that the square RVEs allows for much more diversity in the position of the final vertical crack band compared to the circular RVEs. In addition, the crack bands inside the circular RVEs are more tortuous. For some cases, when an inclusion exists on the RVE edge, a (slight) mixed-mode deformation, instead of a pure mode-I deformation, is obtained as a result of the formulation, which corresponds to a loading direction that is not perpendicular to the crack band.[2] The damage plots of the same RVEs as in Fig. 6.2, at the moment of macroscopic softening, are presented in Fig. 6.6.

6.2.2. Discussion

Although there is a slight difference in the responses of both RVE shapes, the corresponding stress-strain curves are significantly close. A direct consequence of the proposed *mod*-PBCs is that crack bands can only reach the boundary on points with opposing normals.[3] This directly limits the number

[2] Cracks can only cross the RVE boundary on the matrix parts.

[3] Which otherwise would result in unrealistic failure modes, corresponding to a separation in unequal sized parts and issues, similar to the traction and minimal kinematic BCs, would emerge.

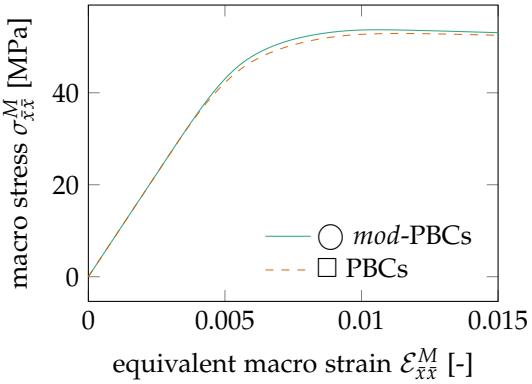

Figure 6.2: Typical stress-strain curve (RVE 1) with *size* 6.

of supported crack band angles on the circular RVE. Additionally, the new framework enforces that the final crack band is always on the matrix part (see Fig. 3.2). When this happens, a (slightly) mixed failure mode is obtained. For some RVEs, where inclusions cross the top and bottom edges, this results in mixed-mode localization, which contributes to the larger spread in peak stress for the small circular RVE sizes compared to the square RVEs (see Fig. 6.3).

However, this effect of slight mixed-mode localization, reduces as the RVE size increases, since there is more fluctuation of matrix and inclusion material points along the edges. Note that for a single crack band orientation ($\theta = 90^\circ$ in this RVE size study), a unique set of nodes exists where the vertical crack band is allowed to cross the edge. Even in the case where there is no inclusion that crosses the edge, this still severely restricts the number of possible localization modes. This is different from the square RVE where a crack band with a certain orientation angle can cross opposing edges at multiple locations (see Fig. 6.5 where there is more diversity in straight crack band positions with the square RVE). This kinematic restriction of the circular RVE, may result in a final failure mechanism that is not the most critical one, which might explain the slightly higher mean values in peak stresses.

Another observation is that macroscopic softening tends to occur at higher strain values with the square RVEs compared to the circular RVEs. As a direct consequence of the formulation, micro cracks are only allowed to cross the edges where the final localization band is assumed to develop. This can be observed from figure Fig. 6.6, where the damage variable ω is plotted for a typical (*size* 6) square and circular RVE. The square RVE does allow for multiple micro cracks along the boundary, as long as they are periodic, whereas the circular RVE only allows cracks between the *opening nodes*. Therefore, even with the improved formulation where a complete softening response is permitted, pre-peak hardening is stiffer for the circular RVE than for the square RVE. In the homogeneous RVE study from Sec. 5, this deviation in peak stress or strain was not present (see Fig. 5.2), because micro cracks did not occur at the boundaries since cracking was triggered in the middle of the specimen through the imperfection and propagated to the edges. The higher pre-peak stiffness is probably the reason for the earlier macroscopic softening with the circular heterogeneous RVE.

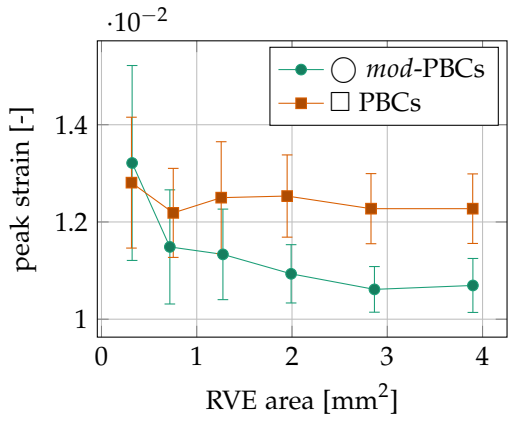

(a) Peak strain

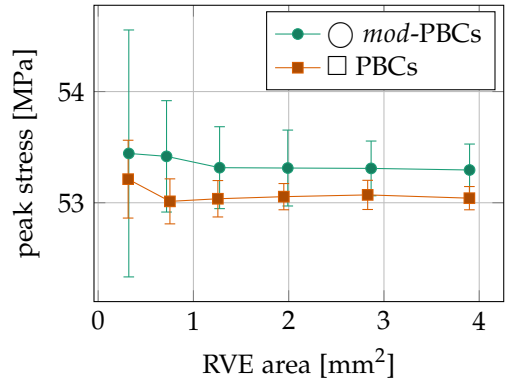

(b) Peak stress

Figure 6.3: Results of the statistical analysis. The sample average plus and minus the sample standard deviation is shown for each RVE size and shape.

6.3. Isotropy study

In this section, a uniaxial strain rate (load case A) and a shear strain rate (load case B) are applied on the RVEs under various angles $\theta(^\circ) \in \{0,5,...,90\}$ (see Tab. 4.1). For this purpose, a circular RVE of *size* 5 is used (see Fig. 6.1).

In the previous section, RVEs with equal volumes (area with unit thickness) were studied, in order to establish a fair comparison in the pre-peak regime. However, in this isotropy study, the circular and the square RVE are loaded to complete failure. It is well known that with classical homogenization, the dissipated energy does not scale with the RVE volume, but with the ratio $\frac{|\Gamma|}{|\Omega|}$ of the macroscopic crack length over the volume [6]. In Sec. 5, where a homogeneous RVE is studied, it is shown that the same deterministic size dependency relation exists for the circular shaped RVE with the novel BCs. Therefore in this study, the ratio $\frac{|\Omega|}{|\Gamma|}$ for both the square and the circular RVE is equal. For this purpose, another square RVE with height $h = 1.5$ mm is generated.[4]

[4]Note that $\gamma = \frac{|\Omega|}{|\Gamma|} = 0.667$ for both RVEs.

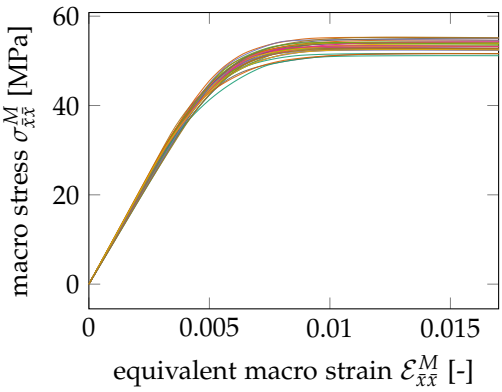

(a) Circular RVE *size* 1

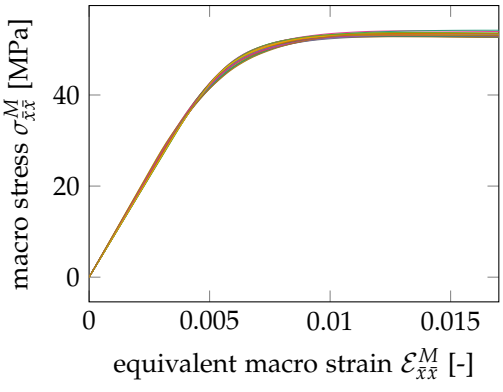

(b) Square RVE *size* 1

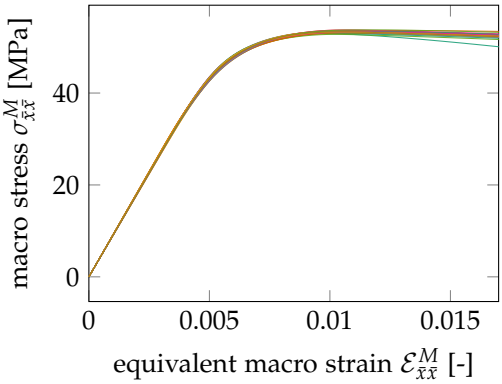

(c) Circular RVE *size* 6

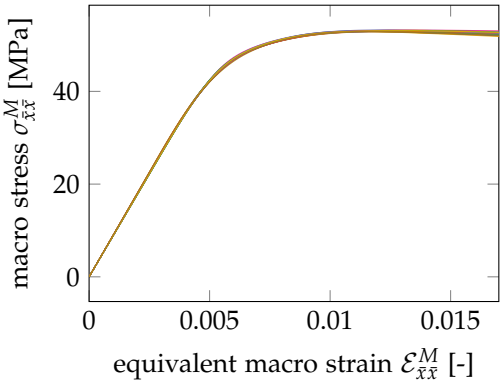

(d) Square RVE *size* 6

Figure 6.4: Stress-strain curves of the smallest (*size* 1) and largest RVEs (*size* 6) with both RVE shapes.

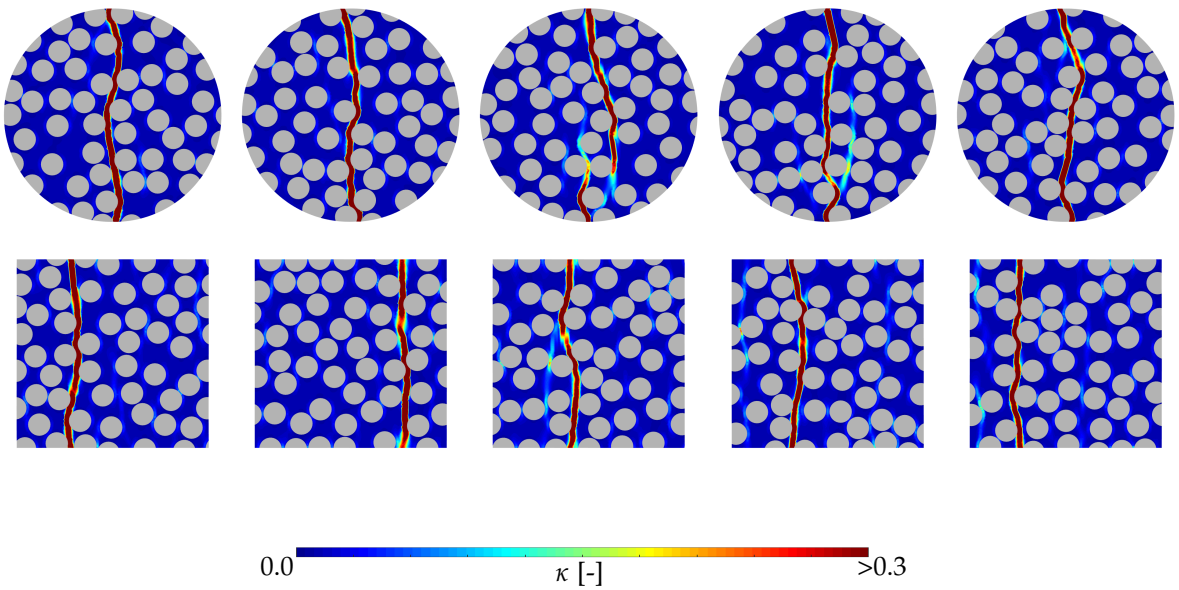

Figure 6.5: Contours of history variable κ with five realizations of RVE *size* 5 at equivalent macroscopic strain $\mathcal{E}^M_{xx} = 0.020$.

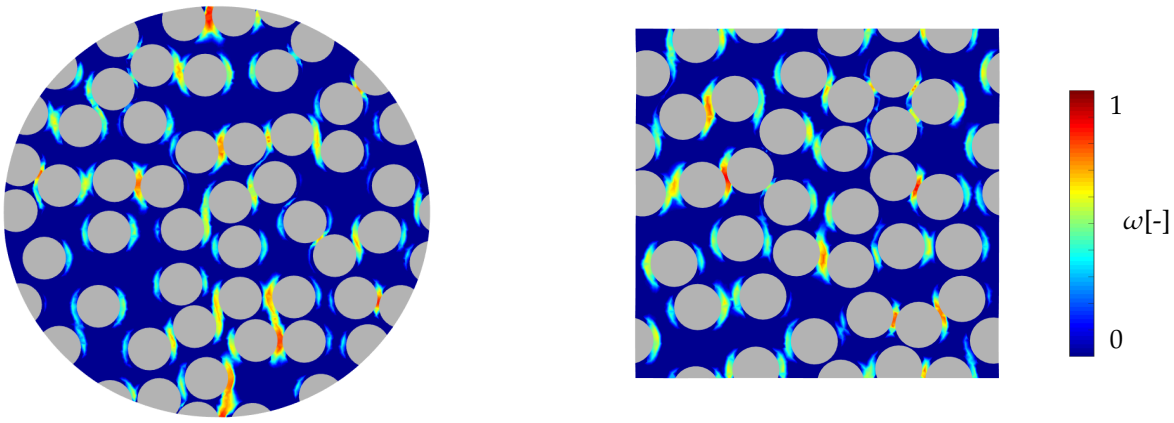

Figure 6.6: Damage plots at the moment of the peak of the circular RVE at equivalent macroscopic strain $\mathcal{E}^M_{xx} = 0.008$.

6.3.1. Results

The development of the crack bands for both the square and the circular RVE, as a result of the load cases A and B under orientation angle $\theta = 25°$, is shown in Fig. 6.13 and Fig. 6.14. It can be observed from these figures that the circular RVE supports single inclined angles, whereas multiple inclined bands appear in the square RVE. Moreover, Fig. 6.14 shows that the sliding of the square and circular RVE in Fig. 6.14 is in different directions. With the circular RVE and the *mod*-PBCs, the normal $\boldsymbol{n}^M_\Gamma$ is not detected on the fly but *a priori* prescribed. Therefore, the sliding direction is always in the direction along $\bar{x}$ (as described in Sec. 4.1), which is not the case with the square RVE where two orthogonal shear band orientations are possible solutions.

The localization patterns for several loading orientation angles θ, are depicted in Fig. 6.9 and Fig. 6.11. It can be observed from these figures that the circular RVE supports inclined (single) localization bands for all orientation angles, while in the square RVE, multiple (periodic) localization bands occur if the orientation angle is not $\theta = 0°$, $45°$ or $90°$.

The stress-strain curves (in local coordinates) as a result of load cases A and B with all loading orientation angles θ are presented in Fig. 6.10 and in Fig. 6.12. For each loading orientation angle θ, the stress values at the peak and after the peak are given in the stress versus the load orientation curves. It can be observed that with both load cases A and B, the scatter in post-peak stresses is far less than with the square RVE. However, with the sliding failure mode, a larger scatter in strength with the circular RVE can be seen. Although a full representativeness study of the circular RVE with mode-II failure is outside the scope of this thesis, some possible reasons for this are discussed in Sec. 6.3.2.

6.3.2. Discussion

In the statistical study from Sec. 6.2, it is observed that the scatter in strength is larger with the circular RVE (see Fig. 6.3), which is probably due to the formulation where *opening nodes* can only exist on the matrix part of the RVE boundary, which in some cases leads to mixed-mode, instead of pure mode-I or mode-II failure. In addition, there are less possibilities for a final failure mode, since

the *opening nodes* are selected *a priori* and are not determined on the fly, which negatively influences the representativeness of the RVE. This effect is more pronounced in pure shear, where multiple (orthogonal) potential shear bands satisfy the same imposed shear deformation via the BCs on the square RVE and where the most critical one, depending on the individual realization of inclusions, becomes the actual final failure mode. With the circular RVE, a single failure mode, with a high chance of not being the most critical one, is enforced by *a priori* selecting the *opening nodes*.

Although the scatter in strength is larger with the circular RVE and the *mod*-PBCs (particularly in mode-II), it can be concluded that it performs better in terms of (post-peak) isotropy than the square RVE with periodic BCs for various load orientation angles θ. The scatter in strength with the circular RVE is related to a single realization and is expected to vanish when the RVE size increases.

6.4. Jump study

In this section, the (unknown) microscopic jump, that is added to the original formulation, is studied in further detail. For this purpose, the same circular RVE as in the previous section is studied in horizontal uniaxial ($\theta = 0°$) loading (see load case A in Tab. 4.1).

The x-component of the micro jump $[\![u]\!]_x$ is monitored in the following. In addition, the horizontal displacement of the node on the boundary of the RVE with the largest x-coordinate and opposite to the fixed node at $(x,y) = (-1,0)$, is tracked and denoted as denoted as $\boldsymbol{u}^{end}$.

6.4.1. Results

Both displacements as functions of the applied equivalent macroscopic strain $\mathcal{E}^M_{xx}$ are shown in Fig. 6.7. From these figures it can be observed that u_x^{end} initially follows the curve $2R\mathcal{E}^M_{xx}$. However, as soon as localization occurs, $[\![u]\!]_x$ becomes nonzero and u_x^{end} starts to trace the line of $\gamma\mathcal{E}^M_{xx}$, and eventually coincides with it. This is a direct consequence of the extra kinematic freedom that is provided by the new formulation Eq. (3.17), which allows for a realistic failure mode when $\boldsymbol{\mathcal{E}}^M = \frac{1}{\gamma}[\![\boldsymbol{u}]\!] \otimes^s \boldsymbol{n}_\Gamma$.

In order to validate the formulation (see Sec. 3.1.3), where only the smooth part of microfluctuations is imposed to be periodic, a 3D plot of the displacement in x-direction is shown in Fig. 6.8. In addition, cross-sections are provided where the x-components of the displacements of the nodes along $y = 0$ are plotted.

6.4.2. Discussion

The 3D plots clearly show that the edges along the boundary are not rigid, nor any weak zones near the corner are cut-off, which are some of the well-known flaws of the classical linear and traction BCs respectively. This study shows that the kinematic restriction provided by surrounding material is realistically taken into account with the new formulation on a circular domain by allowing microfluctuations to exist on the RVE edge. In addition, Fig. 6.8 shows the three contributions superimposed on each other: the smooth microfluctuation, the sharp microfluctuation and the equivalent macroscopic imposed deformation (compare with Fig. 3.1).

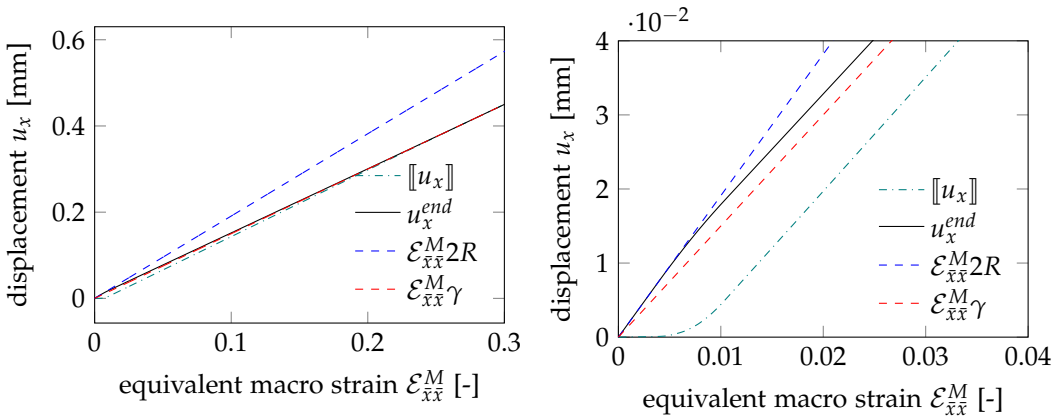

(a) Full curves

(b) Zoomed portion

Figure 6.7: Microscopic jump and displacement of a node with the largest displacement in x as a function of uni-axial macroscopic deformation $\mathcal{E}^M_{xx}$. The red and blue dashed lines are added to the figure as a reference.

6.5. Concluding remarks

The response of the circular RVE with periodic material and with the *mod*-PBCs is very similar to that of the square RVE with periodic BCs in those specific cases when the loading orientation and the material models lead to single localization bands in the square RVE. This verifies the proposed formulation and demonstrates that a realistic kinematic restriction, provided by the material surrounding the RVE, is successfully captured with the *mod*-PBCs.

A slightly stiffer pre-peak hardening response is observed with the circular RVE in comparison to the square RVE. Similar to the response with the *std*-PBCs in Sec. 5, cracks cannot cross the boundary of the RVE. Even with the added kinematic freedom provided by the *mod*-PBCs, there is still some interference of the BCs in the pre-peak branch where edges can not locally crack at positions other than where it is allowed by the formulation at the *opening nodes*. This is different from the square RVE, where edges can locally crack anywhere along the boundary, as long as they appear as periodic pairs. Moreover, with the square RVE, there are multiple options for a potential crack band under 90° angles. This is not the case with the circular RVE where a vertical crack is only supported when *opening nodes* on the top and bottom of the RVE exist. This limits the number of possible failure modes, which often corresponds to a more tortuous crack band. This might contribute to the observed slower decline of the scattering in peak stress compared to the square RVE with periodic BCs. It is expected that upon further increasing the RVE size, this effect diminishes. However, since the statistical representativeness is determined by the number of inclusions in the region of the crack band and not in the overall volume, it is expected that convergence is slower than with the square RVEs.

The most important conclusion is that the circular RVE performs consistently well in terms of post peak isotropy for all load orientation angles, whereas the square RVE over-constrains in the case of inclined loading orientations. This demonstrates that the circular RVE with the *mod*-PBCs outperforms the square RVE with periodic BCs in terms of predicting a transversely isotropic response.

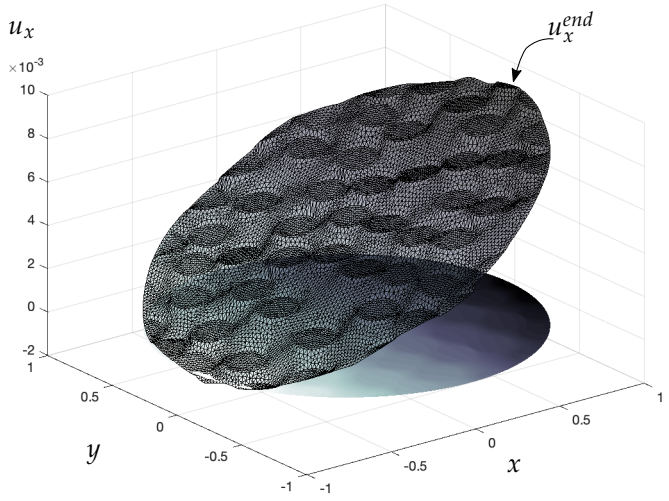

(a) 3D plot before localization

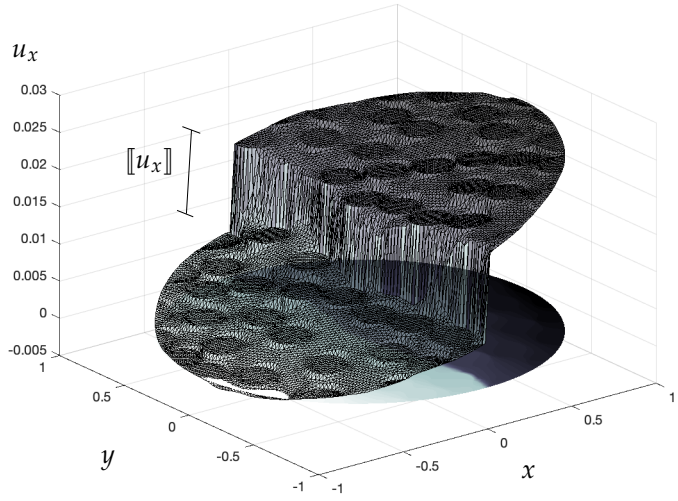

(b) 3D plot after localization

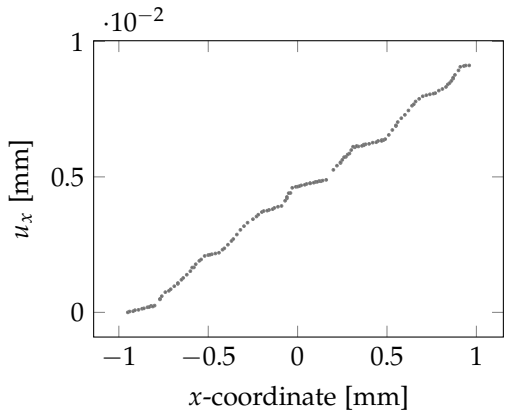

(c) Cross-section before localization

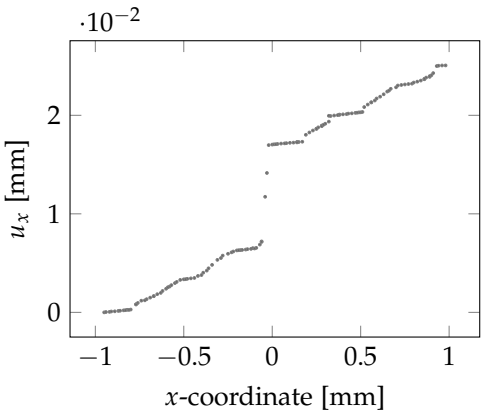

(d) Cross-section after localization

Figure 6.8: Three-dimensional plots and corresponding cross-sections along $y = 0$ of the displacements in x-direction.

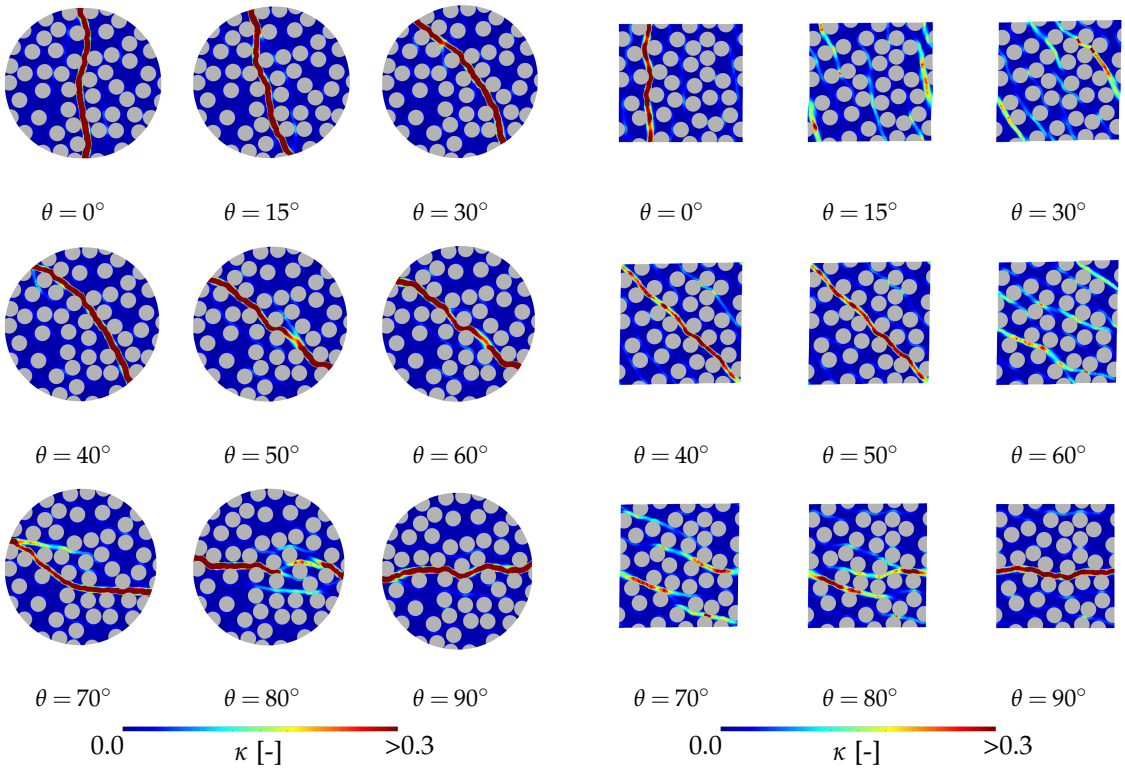

Figure 6.9: RVE crack band patterns corresponding to load case A at $\mathcal{E}^M_{xx} = 0.02$, (deformation $\times 2.5$).

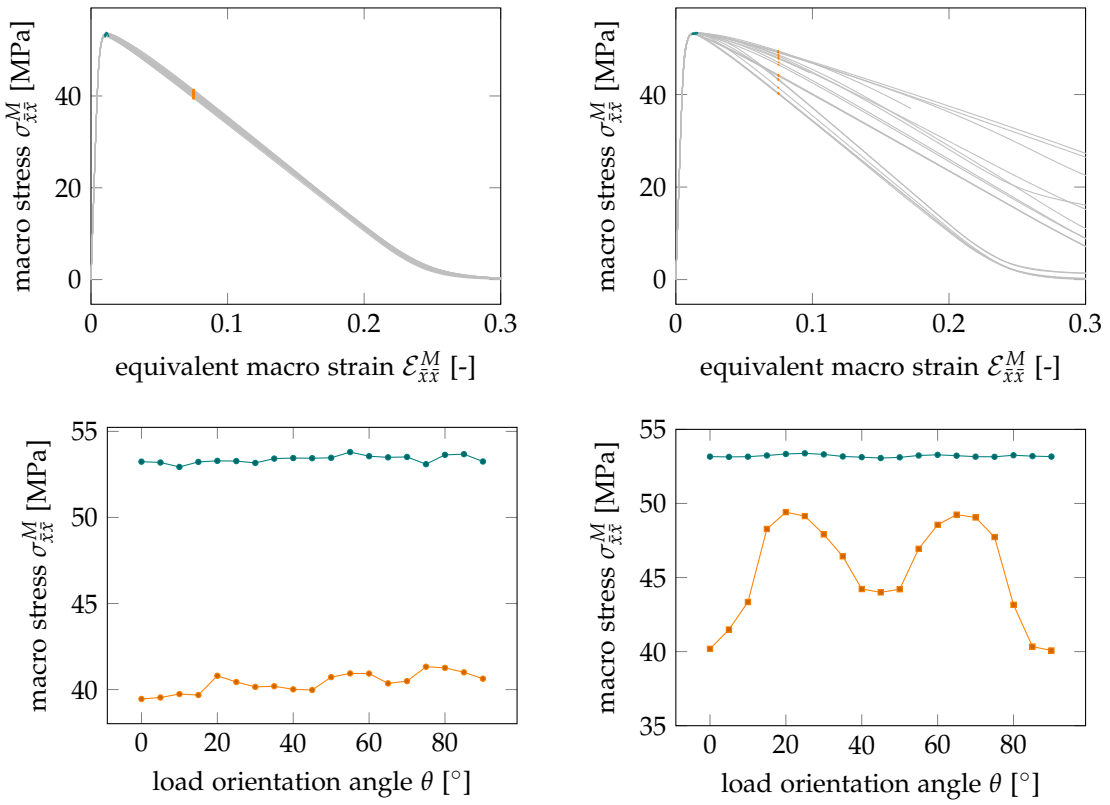

(a) Circular RVE with *mod*-PBCs

(b) Square RVE with PBCs

Figure 6.10: Stress-strain (top) and stress-orientation curves (bottom) corresponding to load case A.

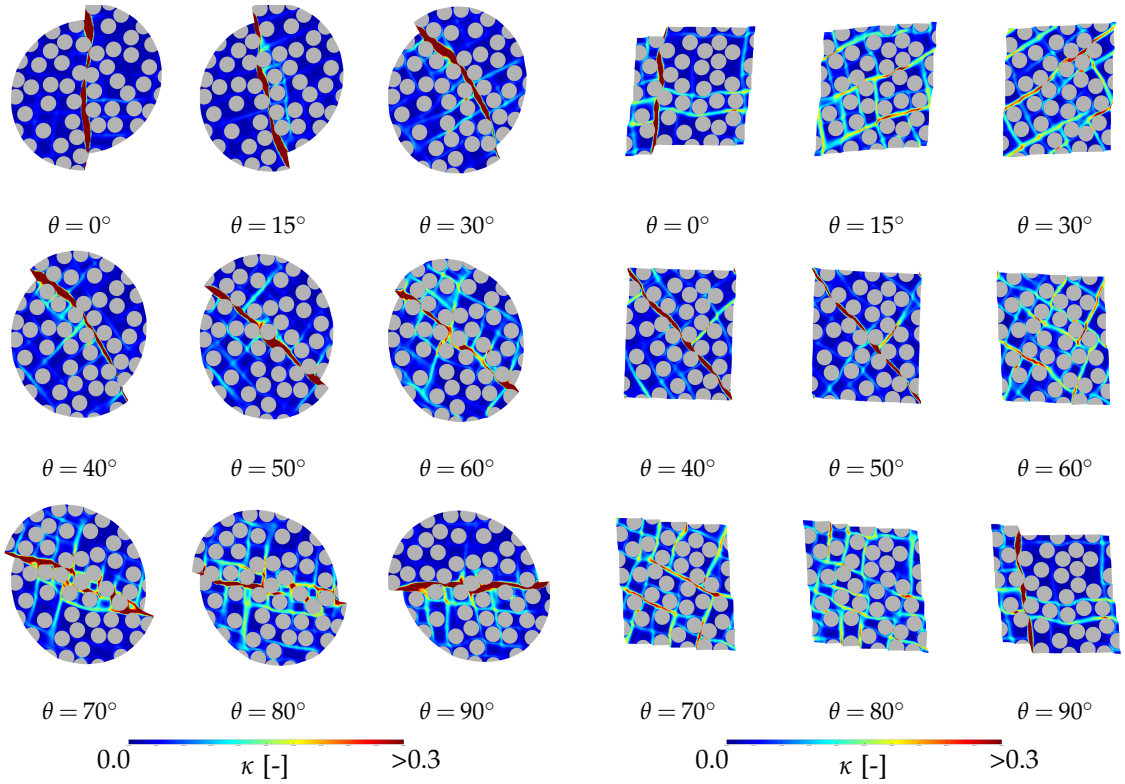

Figure 6.11: RVE crack band patterns corresponding to load case B at $\mathcal{E}^M_{\bar{x}\bar{y}} = 0.04$ (deformation $\times 2.5$).

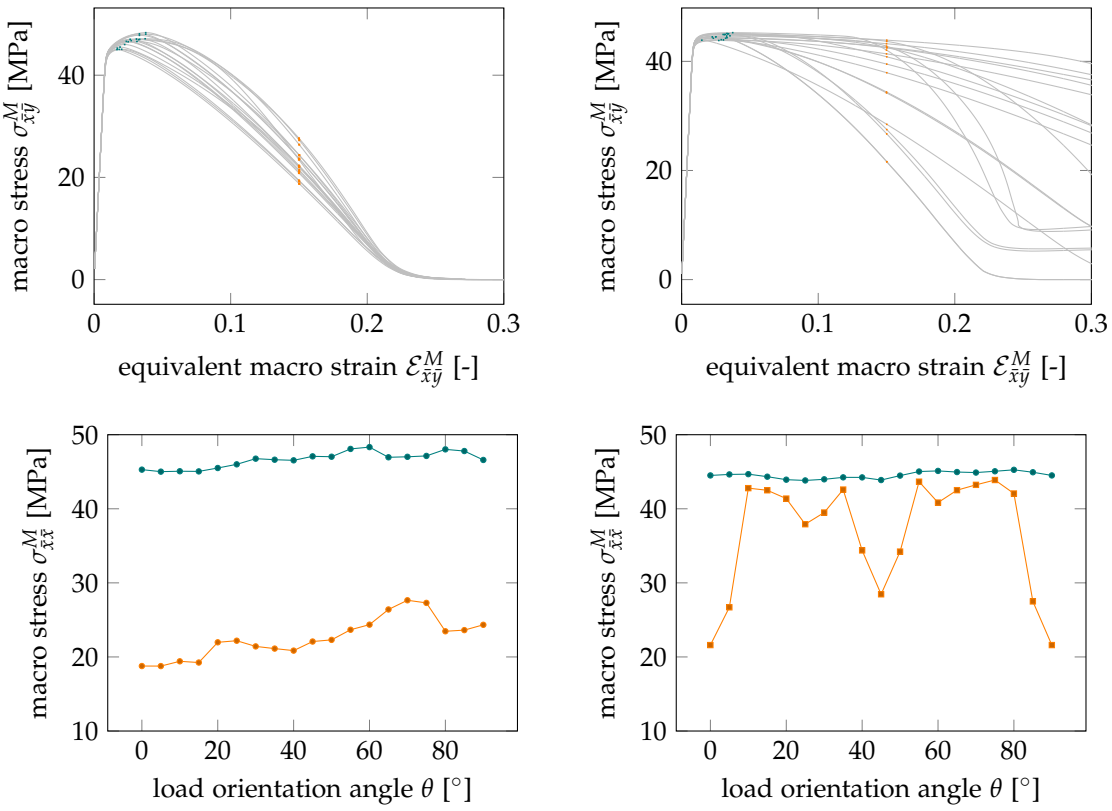

(a) Circular RVE with *mod*-PBCs

(b) Square RVE with PBCs

Figure 6.12: Stress-strain (top) and stress-orientation curves (bottom) corresponding to load case B.

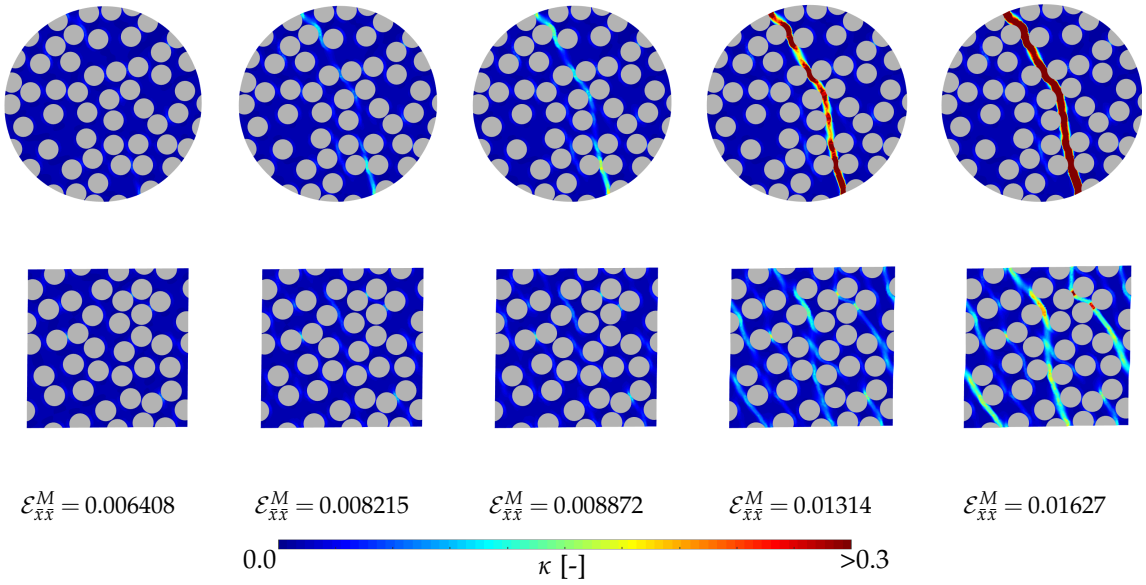

Figure 6.13: Development of localization (mode-I) as a result of load case A and orientation angle $\theta = 25°$ with contour plots of history variable κ (deformation x2.5).

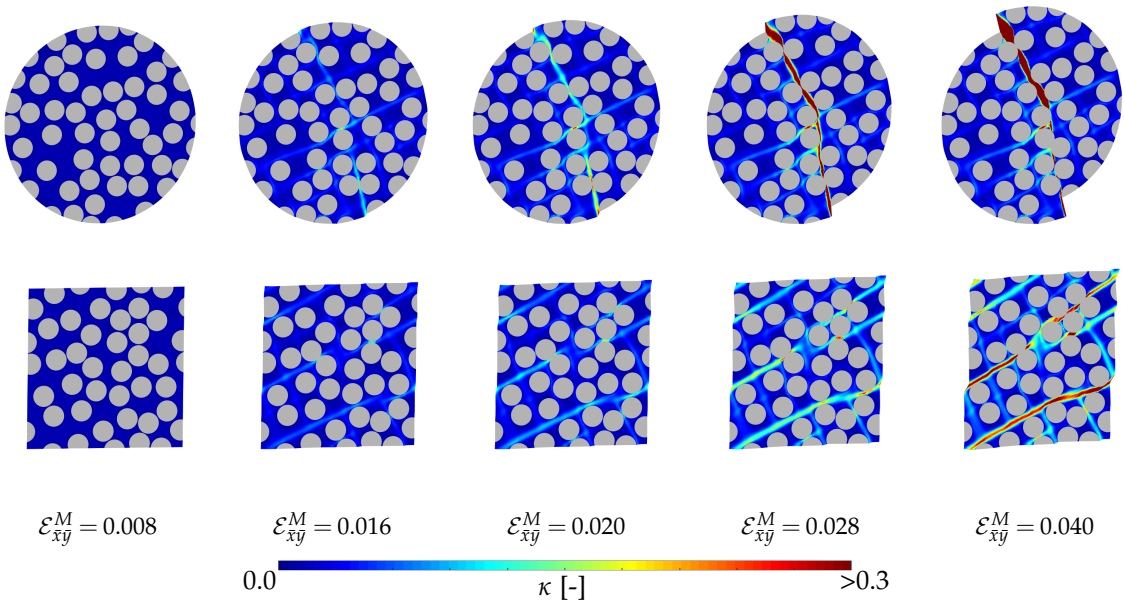

Figure 6.14: Development of localization (mode-II) as a result of load case B and orientation angle $\theta = 25°$ with contour plots of history variable κ (deformation x2.5).

7

Conclusions and recommendations

7.1. Conclusions

It is demonstrated with analytical and numerical examples that the original formulation of periodic BCs on a circular RVE presented in [9], leads to severe over-constraining, since it does not allow for crack bands that cross the RVE boundary. Therefore, the periodic constraints on a circular RVE suppress a full softening response which makes the constraints unsuitable for studying localization problems.

To overcome the aforementioned issue, a modification to the original formulation of the periodic BCs on a circular RVE is proposed, denoted as *modified periodic boundary conditions* (*mod*-PBCs). With this modification, it is demonstrated through numerical simulations with homogeneous and heterogeneous RVEs that the full softening response is recovered *and* that the response is ***fully isotropic***, which was the main objective of this thesis.

Moreover, a new definition of a circular heterogeneous RVE with periodic material is presented, where inclusions are allowed to cross the edge. With a statistical analysis, it is shown that the circular RVE provides almost the same response as the square RVE, when a horizontal uniaxial imposed strain leads to (single) vertical crack bands in both RVEs. However, a slightly stiffer pre-peak hardening response is observed with the circular RVE, since local micro-cracks near the boundary are still suppressed at locations other than where the new formulation allows a dominant final crack to cross the RVE boundary.

Furthermore, there are several advantages of this approach over the other existing remedies (aligned percolation path BCs and aligned weakly periodic BCs in [2] and [23] respectively). In the formulation presented here, there is no need for a rotation or shifting of the microstructure, as is the case with these previously developed approaches. Earlier studies [15] have shown that this implies a mixed coupling of matrix with inclusion points along the edge, which leads to a mis-alignment of inclusions along the RVE boundaries and severely reinforces the edge. Moreover, the approach

presented in this thesis allows for localization by adding an unknown jump to the periodic constraint equations, which does not affect the response before localization and therefore provides a smooth transitioning to a localized state. Although it is not utilized in the numerical examples where the localization angle is *a priori* prescribed, this feature enables the possibility for extending the framework where the correct localization angle is determined on the fly and used to adapt the BCs, without triggering convergence issues due to abrupt changes in the imposed deformations.

7.2. Recommendations

The points on the boundary where the crack band can cross the RVE edge are determined *a priori* in this thesis. Therefore, a logical extension for applications in realistic situations is to determine these points on the fly, which is possible with the presented formulation where the added unknown jump does not affect the response before localization. The approaches used in [2] and [10] employ the Hough transform, which is a well-established image analysis tool that is used in *e.g.* recognizing lines from images, to detect a developing band of highly localized strains. However, it is reported in [10] that the Hough Transform in combination with a material model that exhibits fast strain softening after the limit point, resulted in rapid changes in localization angles, which may trigger convergence issues. Since the micromodel is usually embedded in a multiscale FE^2 framework, a macro jump and corresponding normal vector is provided as soon as localization is detected, *e.g.* by monitoring the eigenvalues of the acoustic tensor. It is expected that the macro jump normal vector can be used to determine the location where the boundary is allowed to crack.

Furthermore, it is observed that the formulation is susceptible to spurious deformation modes. These modes are unrealistic and require more complex localized deformations near the edge. Therefore, these occurred only in a limited number of cases. This is accompanied with localization in multiple elements across the RVE boundary, which is not consistent with the assumption of localization that takes place between two (predefined) nodes on the RVE boundary. Therefore, a material model that is consistent with this assumption resolves this issue. A suitable candidate for this would be a discrete crack model with zero-thickness interface elements.

In this contribution, only single scale analyses are considered where the macroscopic *equivalent* strain is monotonically increased and imposed on the RVEs. An interesting feature of the circular RVE with the new BCs, is that the microscopic (unknown) jump is equal to the macroscopic jump that is imposed on the RVE via Eq. (3.17), because of the choice of γ as $\frac{|\Omega|}{|\Gamma|}$. Therefore, it is expected that RVE size objective (bulk) stress-strain and traction-separation laws can be obtained when the proposed formulation is used in the continuous-discontinuous FE^2 setting. In order to embed the micromodel in this FE^2 framework, consistent tangent operators must be defined.

The loading cases studied in this work are rather simple. Only transverse matrix cracking and sliding are considered failure mechanisms, while de-bonding of the inclusions and the matrix is not modeled. In addition, plasticity is not taken into account. It would be interesting to explore more complex loading scenarios and assess the performance of the circular heterogeneous RVE in representing a realistic composite material.

As a final note, extending the framework to 3D (spherical RVEs) is challenging since *opening edges*

instead of *opening nodes* are not trivially defined on a sphere. However, in order to represent a three dimensional stress state in unidirectional fiber reinforced material, the approach can be used on a 3D slice (cylindrical RVEs).

A

Instable modes

This section briefly covers some of the numerical instabilities that are observed as mentioned in Sec. 4.5. An example of such an instable mode is shown in Fig. A.1a. This mainly occurred in the following cases:

- Bigger sized RVEs
- Irregular Delaunay meshes
- High Poisson's ratio for both the inclusions and the matrix material
- Low fracture energy of the matrix (more brittle response)
- Fibers close to the assigned *opening nodes* on the RVE boundary

Although a thorough study on the origins of this failure mode is outside the scope of this work, some recommendations and suggestions are presented in the sequel.

It can be shown that such a spurious mode is supported by the constraint equations Eq. (3.17). For simplicity, consider the case where $\frac{1}{\gamma}[\![\boldsymbol{u}]\!] \otimes^s \boldsymbol{n}_\Gamma = \boldsymbol{\mathcal{E}}^M$ and therefore $\boldsymbol{u}^+ - \boldsymbol{u}^- = [\![\boldsymbol{u}]\!]$, for all node pairs along the boundary. An arbitrary mode that corresponds to these linear relations, is presented in Fig. A.1. It can be observed that for each node pair, the relative displacement is equal to the jump. Thus, a negative displacement on a negative side of the discontinuity and a positive displacement on the opposite positive side provide a combined positive jump. Although it is highly unphysical, since it requires extreme deformations, it is a solution that is supported by the *mod*-PBCs.

The formulation allows only localization modes where cracks are forced to propagate to the points on the RVE edge where the *opening nodes* are defined (see Fig. 3.2) Because of the occurrence of inclusions close to the opening nodes with small spacings between the edge and the inclusions, extra tortuosity of propagating cracks is demanded for the crack to reach the *opening nodes*. Since the bond is assumed to be perfect (no de-bonding between inclusions and matrix is considered), extra stiffness is introduced thereby increasing the chance that the spurious mode is more critical and consumes less energy than the realistic failure mode.

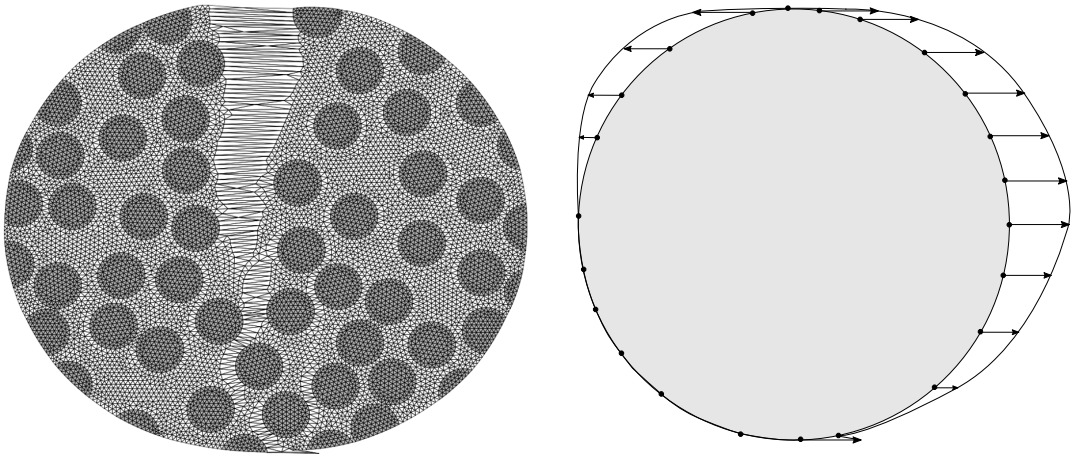

(a) Example of an instable mode

(b) Schematic of an instable mode

Figure A.1: Instable mode.

Figure A.2

In addition, the framework assumes localization in a single row of elements, which enables to define the micro jump as the relative displacement between the nodes of a single element at the edge. However, when a full softening response is prevented by the extra stiffness, energy dissipation starts to occur at multiple locations outside the dominant crack band. If damage starts next to the elements where the *opening nodes* are defined, stiffness locally reduces and the resistance to high strains (see bottom nodes in Fig. A.1) decreases, thereby increasing the chance for obtaining a spurious failure. In addition, due to meshing irregularities, it can happen that a propagating crack reaches the boundary and enters two elements at the same time. In this case, two elements at the boundary are cracked and consequently, the assumption that the micro jump of the RVE is between two nodes of a single element, is incorrect. If localization occurs in an element which has nodes on the RVE boundary that are not the assigned *opening nodes*, then the relative displacement between these nodes must be compensated by the associated nodes on the other side of the RVE. This is exactly what happens, as can be seen from the Fig. A.1 and Fig. A.1a at the top and bottom.

The following is suggested for further studying this numerical instability:

- Use a different material model where discrete cracks are taken into account (for example with zero-thickness interface elements). With this approach, the assumption of a discrete micro jump $[\![\boldsymbol{u}]\!]$ is consistent with the adopted material model.
- Monitor the eigenvalues of the global stiffness matrix. See if a bifurcation point is reached (negative eigenvalues) after the limit point and multiple equilibrium paths exist. The corresponding eigenvectors can give insight in the co-existing solutions and could be used to force the equilibrium path such that the realistic failure mode is obtained.

Bibliography

[1] J. F. Remacle C. Geuzaine. Gmsh: a three-dimensional finite element mesh generator with built-in pre- and post-processing facilities. *International Journal for Numerical Methods in Engineering*, 2009.

[2] E. W. C. Coenen, V. G. Kouznetsova, and M. G. D. Geers. Novel boundary conditions for strain localization analyses in microstructural volume elements. *International Journal for Numerical Methods in Engineering*, 90(1):1–21, 2011. doi: 10.1002/nme.3298.

[3] E. W. C. Coenen, V. G. Kouznetsova, E.Bosco, and M. G. D. Geers. A multi-scale approach to bridge microscale damage and macroscale failure: a nested computational homogenization-localization framework. *International Journal of Fracture*, 178(1-2):157–178, 2012. doi: 10.1007/s10704-012-9765-4.

[4] E. W. C. Coenen, V. G. Kouznetsova, and M. G. D. Geers. Multi-scale continuous–discontinuous framework for computational-homogenization–localization. *Journal of the Mechanics and Physics of Solids*, 60(8):1486–1507, 2012. doi: 10.1016/j.jmps.2012.04.002.

[5] M. G. D. Geers, V. G. Kouznetsova, and W. A. M. Brekelmans. Multi-scale computational homogenization: Trends and challenges. *Journal of Computational and Applied Mathematics*, 234(7):2175–2182, 2010. doi: 10.1016/j.cam.2009.08.077.

[6] I. M. Gitman, H. Askes, and L. J. Sluys. Representative volume: Existence and size determination. *Engineering Fracture Mechanics*, 74(16):2518–2534, 2007. doi: 10.1016/j.engfracmech.2006.12.021.

[7] R. Glüge. Generalized boundary conditions on representative volume elements and their use in determining the effective material properties. *Computational Materials Science*, 79:408–416, 2013. doi: 10.1016/j.commatsci.2013.06.038.

[8] R. Glüge and M. Weber. Numerical properties of spherical and cubical representative volume elements with different boundary conditions. *Technische Mechanik*, 2012.

[9] R. Glüge, M. Weber, and A. Bertram. Comparison of spherical and cubical statistical volume elements with respect to convergence, anisotropy, and localization behavior. *Computational Materials Science*, 63:91–104, 2012. doi: 10.1016/j.commatsci.2012.05.063.

[10] J. Goldmann, J. Brummund, and V. Ulbricht. On boundary conditions for homogenization of volume elements undergoing localization. *International Journal for Numerical Methods in Engineering*, 113(1):1–21, 2017. doi: 10.1002/nme.5597.

[11] R. Hill. A self-consistent mechanics of composite materials. *Journal of the Mechanics and Physics of Solids*, 13(4):213–222, 1965. doi: 10.1016/0022-5096(65)90010-4.

[12] V. Kouznetsova, M. G. D. Geers, and W. A. M. Brekelmans. Multi-scale constitutive modelling of heterogeneous materials with a gradient-enhanced computational homogenization scheme. *International Journal for Numerical Methods in Engineering*, 54(8):1235–1260, 2002. doi: 10.1002/nme.541.

[13] V. G. Kouznetsova. *Computational homogenization for the multi-scale analysis of multi-phase materials*. PhD thesis, Technische Universiteit Eindhoven, 2002.

[14] F. Larsson, K. Runesson, S. Saroukhani, and R. Vafadari. Computational homogenization based on a weak format of micro-periodicity for RVE-problems. *Computer Methods in Applied Mechanics and Engineering*, 200(1-4):11–26, 2011. doi: 10.1016/j.cma.2010.06.023.

[15] E. Giesen Loo and F. P. van der Meer. Stress-controlled weakly periodic boundary conditions: Axial stress under varying orientations. *International Journal for Numerical Methods in Engineering*, 121(19):4458–4470, 2020. doi: 10.1002/nme.6441.

[16] J. J. C. Remmers M. A. Crisfield, C. V. Verhoosel, and R. de Borst. *Nonlinear Finite Element Analysis of Solids and Structures*. WILEY, 2012. ISBN 0470666447.

[17] S. Dj. Mesarovic and J. Padbidri. Minimal kinematic boundary conditions for simulations of disordered microstructures. *Philosophical Magazine*, 85(1):65–78, 2005. doi: 10.1080/14786430412331313321.

[18] C. Miehe. Computational micro-to-macro transitions for discretized micro-structures of heterogeneous materials at finite strains based on the minimization of averaged incremental energy. *Computer Methods in Applied Mechanics and Engineering*, 192(5-6):559–591, 2003. doi: 10.1016/s0045-7825(02)00564-9.

[19] V. P. Nguyen. *Multiscale failure modelling of quasi-brittle materials*. PhD thesis, Delft University of Technology, 2011.

[20] V. P. Nguyen, M. Stroeven, and L. J. Sluys. Multiscale continuous and discontinuous modeling of heterogeneous materials: a review on recent developments. *Journal of Multiscale Modelling*, 03 (04):229–270, 2011. doi: 10.1142/s1756973711000509.

[21] J. Oliver, M. Caicedo, E. Roubin, A. E. Huespe, and J. A. Hernández. Continuum approach to computational multiscale modeling of propagating fracture. *Computer Methods in Applied Mechanics and Engineering*, 294:384–427, 2015. doi: 10.1016/j.cma.2015.05.012.

[22] E. Svenning, M. Fagerström, and F. Larsson. Computational homogenization of microfractured continua using weakly periodic boundary conditions. *Computer Methods in Applied Mechanics and Engineering*, 299:1–21, 2016. doi: 10.1016/j.cma.2015.10.014.

[23] E. Svenning, M. Fagerström, and F. Larsson. Localization aligned weakly periodic boundary conditions. *International Journal for Numerical Methods in Engineering*, 111(5):493–500, 2017. doi: 10.1002/nme.5483.

[24] E. Svenning, F. Larsson, and M. Fagerström. Two-scale modeling of fracturing solids using a smeared macro-to-micro discontinuity transition. *Computational Mechanics*, 60(4):627–641, 2017. doi: 10.1007/s00466-017-1426-z.

[25] E. Svenning, F. Larsson, and M. Fagerström. A two-scale modeling framework for strain localization in solids: XFEM procedures and computational aspects. *Computers & Structures*, 211:43–54, 2019. doi: 10.1016/j.compstruc.2018.08.003.

[26] C. V. Verhoosel, J. J. C. Remmers, M. A. Gutiérrez, and R. de Borst. Computational homogenization for adhesive and cohesive failure in quasi-brittle solids. *International Journal for Numerical Methods in Engineering*, 83(8-9):1155–1179, 2010. doi: 10.1002/nme.2854.